Metastability and Nondislocation-Based Deformation Mechanisms of the Flem Eclogite in the Western Gneiss Region, Norway

Yi Cao[1,2], Jinxue Du[3], Munjae Park[2], Sejin Jung[2], Yong Park[2], Dohyun Kim[2], Seungsoon Choi[2], Haemyeong Jung[2], and Håkon Austrheim[4]

[1]State Key Laboratory of Geological Processes and Mineral Resources, School of Earth Sciences, China University of Geosciences, Wuhan, China, [2]Tectonophysics Laboratory, School of Earth and Environmental Sciences, Seoul National University, Seoul, South Korea, [3]School of Earth Sciences and Resources, China University of Geosciences, Beijing, China, [4]Physics of Geological Processes, University of Oslo, Oslo, Norway

Abstract The eclogite in the Flem Gabbro from Flemsøya Island of the Western Gneiss Region in Norway contains atypical eclogitic minerals, such as olivine and orthopyroxene, and can be texturally divided into weakly deformed massive eclogite (MEC) and strongly deformed foliated eclogite (FEC). Based on phase equilibria modeling, peak metamorphic pressure-temperature conditions of ~600–750 °C and ~1.0–2.5 GPa and ~700–820 °C and ~2.7–3.7 GPa are recorded in MEC and FEC, respectively. These different pressure-temperature conditions between MEC (high-pressure, HP) and FEC (ultrahigh-pressure, UHP) in the same outcrop reflect deformation-enhanced eclogitization metamorphism (HP to UHP transition) via the addition of external water during subduction/burial to early exhumation stages and metastable preservation of the HP MEC assemblage at UHP condition due to the local lack of deformation and fluid access at the deep subduction interface or around Moho beneath continental collision zone. Based on the mineral microstructures, nondislocation-based creep mechanisms—such as diffusion creep, grain and phase boundary sliding, and rigid-body-like rotation—play dominant roles in governing the deformation features of FEC and developing the crystal preferred orientations of its major constituent minerals. These deformation mechanisms could considerably affect the interplate coupling at the subduction interface or the rheological strength of Moho beneath continental collision zones. Therefore, the effects of metastability-based (i.e., preservation of low-pressure assemblages at HP conditions) and contributions of nondislocation-based creep mechanisms should be included in the future geodynamic and petrological simulations of subduction and collision processes.

Plain Language Summary Eclogite is a unique metamorphic rock that forms at high pressure and indicates deeply subducted crust or thick continent crust around Moho depth. Under tectonic forces, such high-pressure rocks can be exhumed and exposed in some current orogenic belts, such as the eclogite in the Flem Gabbro from Flemsøya Island of the Western Gneiss Region in Norway. Based on an integrated study, we acquired two key findings from this eclogite. First, due to lack of deformation and fluid access, the weakly deformed massive type of eclogite is metastable at the higher pressure and temperature condition where strongly deformed foliated type of eclogite is stable. Second, mineral microstructures suggest that the deformation is mainly accommodated by nondislocation-based creep mechanisms, such as diffusion creep, grain and phase boundary sliding, and rigid-body-like rotation, which produce weak crystal preferred orientations of major phases. The influences of metastability and nondislocation-based creep mechanisms are believed to be important but rarely addressed in the current geodynamic and petrological simulations of subduction and collision processes. This study points out some concerns and directions for future numerical modeling studies.

1. Introduction

The subduction interface or channel is a narrow zone (or plate boundary) sandwiched between subducting crust (footwall) and overriding plate (hanging wall). Most of the tectonic slip, strain, and energy

related to plate convergence are accommodated and released in this tectonically active and weak zone by inhomogeneous and localized deformation such as seismic slip in the coupled seismogenic zone at shallow depth, semibrittle slip in the partially coupled zone at intermediate depth (brittle-ductile transition zone), and aseismic creep in the decoupled zone as well as intermediate-depth earthquakes at depth (e.g., Andersen & Austrheim, 2006; Angiboust et al., 2015; Audet & Kim, 2016; Austrheim, 2013; Austrheim & Boundy, 1994; Bachmann et al., 2009; Duarte et al., 2015; Isacks et al., 1968; John et al., 2009; Jung et al., 2004; Lund & Austrheim, 2003; Oleskevich et al., 1999; Tichelaar & Ruff, 1993; Wassmann & Stockhert, 2013).

Eclogite, common as a major constituent of the subduction interface, is derived from mafic components (e.g., basalt, diabase, and gabbro) of the subducting crust that experienced high-pressure-ultrahigh-pressure (HP-UHP) metamorphism at depths greater than ~45 km (MacGregor & Manton, 1986; Peacock, 1993). In outcrops, eclogite often behaves as hard block wrapped in a soft matrix that consists of metasediments, serpentinite, and other weak metamafic rocks (e.g., greenschist, amphibolite, and blueschist; oceanic-type mélange) (e.g., Angiboust et al., 2011; Davis & Whitney, 2006; Du et al., 2014; Ernst, 2016; Laurent et al., 2016; Neufeld et al., 2008; Song et al., 2007; Spandler et al., 2008) or surrounded by weak lithologies such as gneiss, marble, and quartzite (continental-type mélange) (e.g., Baldwin et al., 2004; Cuthbert et al., 2000; Kaneko et al., 2000; Liou et al., 2000; Schulmann et al., 2009; Yang et al., 2002). However, the notion of continental subduction channel setting comprising eclogite was challenged in some regions, because the so-called "mélange" may also represent a processed Moho zone beneath the continental collision belts (see review of Austrheim, 2013).

Abundant observations on natural samples show that eclogite is not uniform and has various microstructures in outcrops and/or specimens (e.g., massive vs. foliated, coarse-grained vs. fine-grained, and fresh vs. retrograded; e.g., Boundy et al., 1992; Cao et al., 2011; Engvik et al., 2007; Kurz et al., 2004; Park & Jung, 2019; Soldner et al., 2017). These microstructural differences imply that the mechanical strength of eclogite is variable and related to the constituting mineral assemblages. This correlation raises a "chicken-and-egg" question about how deformation could affect HP-UHP metamorphism or metasomatism and vice versa (Brodie & Rutter, 1985; Thompson et al., 1985). Specifically, does the deformation reshape the rock microstructure such that the subsequent metamorphic equilibrium can be modulated or does the metamorphic reaction modify the rheology of the mineral assemblage (strengthen or weaken the rock), ensuring that the deformation can be regulated?

The deformation mechanisms and the geneses of the crystal preferred orientations (CPOs) for the major minerals in eclogite have long been discussed. It is generally considered that dislocation creep is the dominant mechanism to cause the mineral CPOs in eclogite, whereas some proposed that diffusion creep may also be essential in some specific situations (see a recent review by Keppler (2018)). However, the roles of grain boundary processes such as grain boundary sliding (GBS) and grain rotation on the deformation of eclogite are still not well known, even though their importance is being recognized in peridotite (Hansen et al., 2011; Maruyama & Hiraga, 2017a; Précigout & Hirth, 2014; Wang et al., 2013; Zhao et al., 2019).

The eclogites in the Flem Gabbro from Flemsøya Island in the Nordøyane UHP terrane of the Western Gneiss Region (WGR) in Norway are excellent cases to study the above issues. These eclogites may once have been situated in a continental subduction channel or continental root zone (around Moho) owing to continental subduction and collision (see review of Austrheim (2013)). Unlike typical eclogite, these eclogites are rich in olivine because they are derived from an olivine gabbro protolith (Mørk, 1985). In the field, the eclogites are distributed within migmatite gneiss (country-rock eclogite suite, Types 2 and 3) and gabbro (gabbro-eclogite suite, Type 1; see classifications by Mørk, 1985). The studied eclogite samples are of Type 1 and show several types of deformation microstructures. We analyzed and compared the microstructural and metamorphic characteristics of these variously deformed eclogites. The results provide valuable insights into the relationships between HP-UHP metamorphism, presence of fluid, and ductile deformation and the deformation mechanisms of mafic-ultramafic components at the subduction interface or around continental Moho beneath collision zones.

2. Tectonic and Geological Setting

2.1. WGR

The WGR of Norway is one of the largest and best-exposed HP-UHP terranes in the world. The Caledonian UHP terrane (~5,000 km^2) is surrounded to the north, east, and south by HP rocks (~30,000 km^2). The WGR consists of Proterozoic gneisses, often referred to as Western Gneiss Complex (WGC), and a stack of overlying continental and oceanic allochthons (Figure 1a; Hacker et al. (2010)). The WGR and associated Caledonian orogen were formed by the successive events as closure of the Iapetus Ocean (~430–410 Ma), Baltica-Laurentia collision and associated westward subduction of the Baltica basement (~425–400 Ma), and final extensional orogenic collapse (~400–380 Ma) (Andersen, 1998; Andersen et al., 1991; Hacker, 2007; Hacker & Gans, 2005; Kylander-Clark et al., 2007; Tucker et al., 2004; Walsh et al., 2007).

Based on the pressure-temperature (P-T) estimates, three UHP domains are recognized along the west Norwegian coast from south to north (Nordfjord, Sørøyane, and Nordøyane), separated by Baltica basement gneisses that lack evidence for UHP (Figure 1b; see Hacker et al., 2010). The increase in peak metamorphic P-T conditions coastward is consistent with northwestward subduction. The lowest and highest peak P-T conditions are preserved in the Nordfjord (700–800 °C and 2.8–3.0 GPa, see Wain et al., 2000, and Cuthbert et al., 2000) and Nordøyane (>800 °C and 3.0–4.0 GPa; see Terry et al., 2000, Carswell et al., 2006, and Butler et al., 2013) UHP domains, respectively.

2.2. Nordøyane UHP Domain

The Nordøyane UHP domain can be divided into three structural-tectonic segments (northern, central, and southern) that are separated by major shear zones (Figure 1c; see Terry & Robinson, 2003). These lithotectonic segments are dominated by granodioritic to dioritic gneisses of the Baltica basement that are overlain by remnants of Caledonian thrust nappes (Sætra and Blåhø nappes). Evidence for UHP metamorphism has been reported from the northern segment of Nordøyane such as microdiamonds in garnet-biotite-kyanite gneiss from Fjørtoft (Dobrzhinetskaya et al., 1995); coesite and/or polycrystalline quartz pseudomorphs in eclogite from Harøya (Butler et al., 2013), Fjørtoft, and Flemsøya (Cuthbert et al., 2000; Terry et al., 2000); thermobarometric estimates for orthopyroxene eclogite in Fjørtoft and Otrøy (Carswell et al., 2006), and microdiamonds and majoritic garnet in peridotite from Fjørtoft and the nearby mainland (van Roermund & Drury, 1998; Vrijmoed et al., 2008). The HP-UHP metamorphism occurred at ~415–410 Ma (Krogh et al., 2011) and was subsequently overprinted by granulite to lower amphibolite facies metamorphism with local partial melting at ~395 Ma during exhumation (Krogh et al., 2011; Tucker et al., 2004).

2.3. NW Flemsøya and Flem Gabbro

The NW Flemsøya structurally belongs to the northern segment of the Nordøyane UHP domain (Figure 1c) and is lithologically dominated by granitic, dioritic, and augen migmatitic gneisses crosscut by variably eclogitized gabbro (Figure 1d; Mørk (1985)). The Flem Gabbro or Sandvikhaugane Gabbro as defined by Mørk (1985) is the largest gabbro block in NW Flemsøya. This gabbro is variably eclogitized (Type-1 eclogite as defined by Mørk, 1985) and shows two sets of nearly vertical foliation with NW and NE strike and eastward trending and steeply plunging lineation that formed at eclogite facies conditions (Terry & Robinson, 2004). The nearby migmatitic gneisses that enclose the eclogite (Types 2 and 3) and gabbro present later well-developed granulite to amphibolite facies assemblages and fabrics due to top-to-W shearing (Mørk, 1985).

In a previous petrological study, the peak metamorphic P-T conditions of these types of eclogite were constrained to be 1.5–2.0 GPa and 750 ± 60 °C in this area (Mørk, 1985). The age of the eclogite facies metamorphism was determined to be 400 ± 16 Ma using a three-point (garnet-clinopyroxene-whole rock) Sm-Nd isochron (Mørk & Mearns, 1986) and was later recalculated to be 410 ± 16 Ma (Root et al., 2004). Krogh et al. (2011) more recently reported a similar eclogitization age of 410 ± 2 Ma for Flem Gabbro eclogite based on U-Pb zircon dating. Besides, they also determined the primary age of the gabbro (age of igneous crystallization) and timing of amphibolite facies metamorphism (age of pegmatite crystallization) to be 1,255 ± 2 and 396 ± 4 Ma, respectively (Krogh et al., 2011).
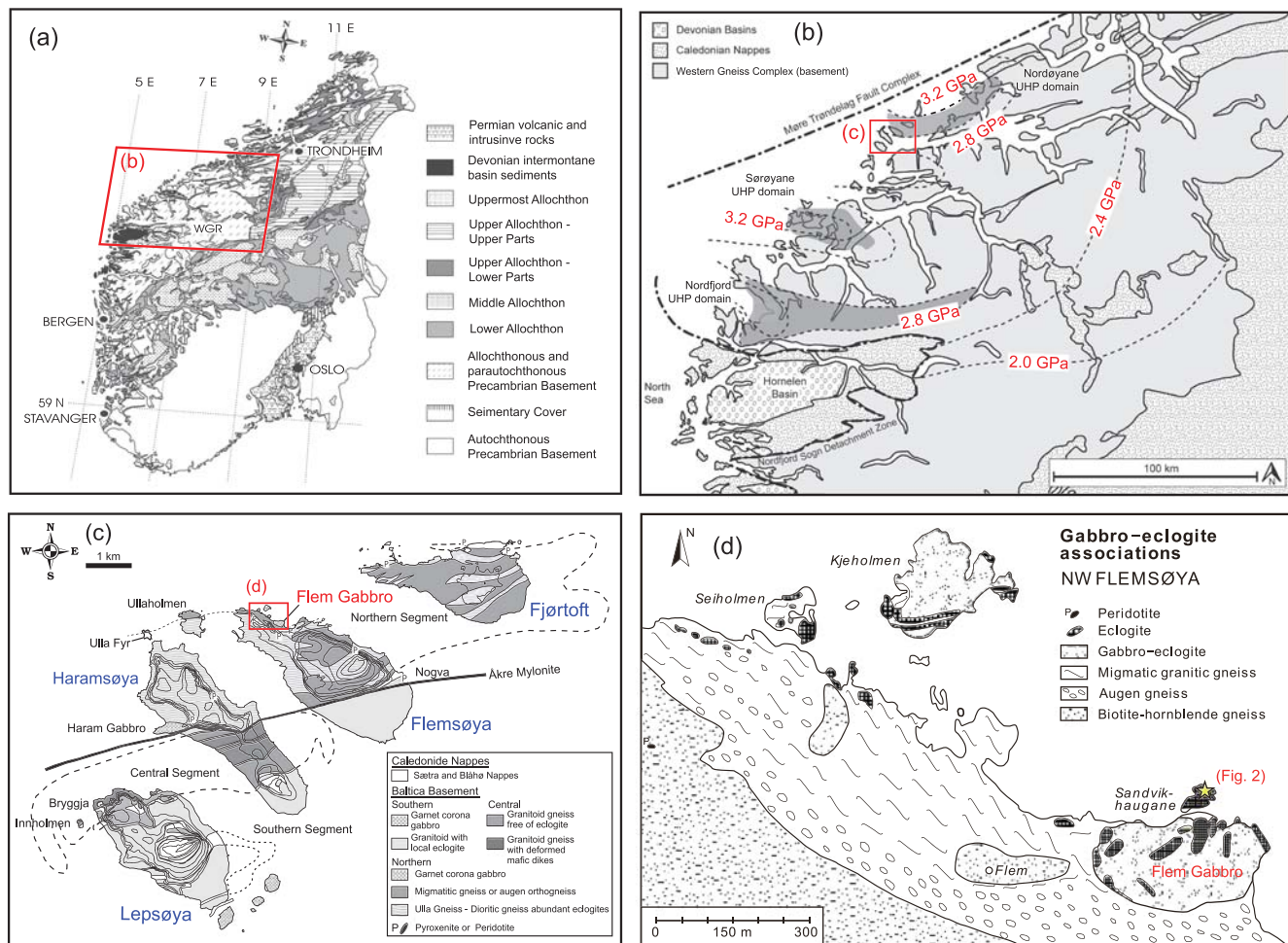
Figure 1. (a) Generalized tectonostratigraphic map of the southern part of the Scandinavian Caledonides modified after Terry and Robinson, 2003. The red parallelogram indicates the location of WGR. (b) Geological map showing the WGR that consists of WGC basement (light gray) overlain by allochthons (modified after Renedo et al., 2015, and Hacker et al., 2010). The dark gray area denotes three UHP domains along the western coast of the WGC, from south to north: Nordfjord, Sørøyane, and Nordøyane. The dashed lines are isobars of metamorphic pressures displaying a northwestward increasing P-T trend. The studied region (Nordøyane) is indicated by a red rectangle. (c) Generalized geological map of the Nordøyane UHP terrane showing the major lithotectonic units (modified after Terry & Robinson, 2003). The studied eclogites are situated in the Flem Gabbro in the NW part of Flemsøya Island. (d) Geological map of the NW part of Flemsøya (inset in Figure 1c) showing the distribution of two eclogite suites (within gabbro and within migmatite). The studied eclogites are within gabbro at the northernmost margin of the Flem Gabbro (indicated by a yellow star, see Figure 2; modified after Mørk, 1985, and Terry & Robinson, 2004).

3. Field Structures of Flem Eclogite

The studied eclogite samples are from the northernmost margin of the Flem Gabbro (Figure 1d). This part of the gabbro body is almost completely eclogitized and characterized by fresh eclogite with various deformed microstructures (Figure 2). The eclogite is strongly sheared and displays continuous and steep foliation subparallel to the strike of the block (Figures 2a–2c). Weakly deformed massive eclogite (MEC) occurs as lenticular relic cores with tapering tails within strongly deformed foliated eclogite (FEC; Figures 2b and 2e). The boundaries between MEC and FEC are often sharp and marked by decimeter-scale mylonitic shear zones (Figures 2d and 2e), indicating a large strain gradient or heterogeneous deformation.

4. Method

4.1. Sampling and Thin Section Preparation

Seven of total 14 samples (two MEC and five FEC samples) collected from the eclogite outcrop were selected for this study (their sampling locations are shown in Figures 2b–2e). For the FEC specimens showing clear
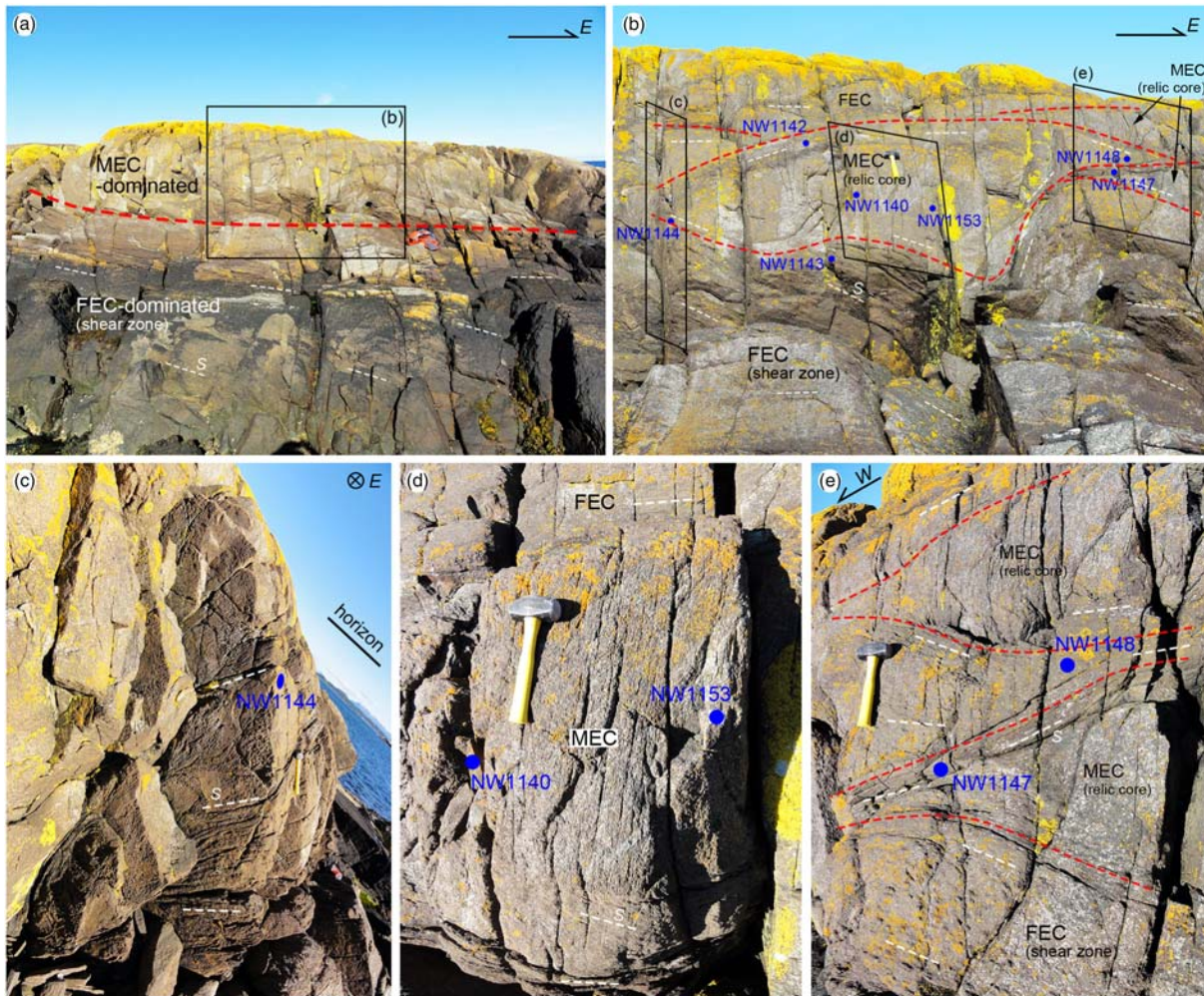
Figure 2. Field structures of the studied eclogite block. (a) Far view of the nearly EW striking eclogite body. The thick red dashed line indicates the approximate boundary separating MEC- and FEC-dominated regions. The thin white dashed line denotes the orientation of the foliation (*S*) within the FEC. (b) Enlarged view of a MEC-dominated region (inset in (a)) in which the boundaries between MEC and FEC are delineated by thin red dashed lines. (c) Strike-perpendicular view at the tail end of a MEC region (inset in (b)) showing steeply dipping foliation in FEC. (d) View of a MEC relic and its nearby FEC (inset in (b)). Note the sharp boundaries between MEC and FEC. (e) Strike-oblique view of several stacking MECs (inset in (b)). The boundaries of lens-shaped MEC are locally represented by decimeter-scale mylonitic shear zones. The sampling locations of the studied eclogite are indicated with blue solid circles. The Samples NW1140 and NW1153 are MEC; the others are FEC.

foliation and lineation, thin sections were cut parallel to the lineation and perpendicular to the foliation (i.e., *XZ* plane). For the MEC specimens whose foliation and lineation are hardly recognizable in the specimen, we took the foliation of their adjacent FEC as the structural reference for MEC and cut the thin sections parallel to this reference plane. We denoted this reference plane as *X′Y′* plane hereafter, in which *X′* and *Y′* are the apparent lineation determined by the shape preferred orientations (SPOs) of olivine in the thin sections and the other direction perpendicular to the apparent lineation on the *X′Y′* plane, respectively. All thin sections were finely polished using 1-μm diamond paste and SYTON (0.06-μm colloidal silica) before further analyses.

4.2. Electron Backscattered Diffraction and Data Treatment

The mineral orientation data were measured using an electron backscattered diffraction (EBSD) system installed at a Quanta 450 Field Emission Scanning Electron Microscope at the State Key Laboratory of Geological Processes and Mineral Resources in the China University of Geosciences (Wuhan), China, and using the EBSD system with a Symmetry Detector (Oxford Instrument) attached to Field Emission

Scanning Electron Microscope (JSM-7100F) at the School of Earth and Environmental Sciences in Seoul National University in Korea. The XZ plane and apparent $X'Y'$ plane thin sections were analyzed for FEC and MEC, respectively. The operational settings of the EBSD system include an acceleration voltage of 20 kV, working distance of 25 mm and a spot size of 60 in a low-vacuum mode. To acquire the orientation information in various spatial scales and resolutions, we conducted EBSD mapping over different-sized rectangular domains in the thin sections with multiple step sizes depending on grain size and domain area. Generally, large and small step sizes of 15–50 and 4–5 μm were applied for large (~1/2–2/3 of entire thin section area, totaling ~2–7 cm^2) and small (~0.1–0.3 cm^2) domains, respectively. Except large-area domain mapping, the raw indexing rates are higher than 80% in most small-area domain mapping.

To get a clean EBSD data set, before grain constructions and CPO analyses, inaccurate indexing points (mean angular deviation, >0.8°) and wild spikes (point clusters <3–5 pixels) were eliminated. The CPOs of minerals were calculated using the orientation distribution functions, which were derived from the orientation data. The mean orientations of individual grains averaged from all indexed points in a grain were plotted at pole figure, yielding namely one-point-per-grain CPO. A "de la Vallée Poussin" kernel half width of 10° was applied to calculate orientation distribution functions and to estimate the CPO strength (i.e., J-index, ranging from 1 to ∞) (Bunge, 1982). For comparison, another index, M-index, ranging between 0 and 1, was also used for quantifying the CPO strength (Skemer et al., 2005).

To construct the grains, the grain boundaries were customarily defined by the neighboring pixels that have misorientation angles greater than 10° and the influence of unindexed points on segmenting a single grain into several smaller patches was removed. Besides, before analyzing the grain fabrics, such as grain size, grain shape, and grain orientation, the grains locating at the map boundaries and having unindexed areas larger than 50% of their constructed grain areas were also excluded. The grain size was calculated as equivalent circular diameter, namely, the diameter of a circle that has the same area with the actual grain. The aspect ratio was defined by the length ratio of long to short axes in the best fitting ellipse, while the angle between the long axis and a given reference direction (e.g., foliation or lineation) gave the orientation of the grain. The sinuosity of grain boundaries was quantified by shape factor, which is the perimeter ratio of an actual grain to a circle with the same area. The mis-to-mean orientation (M2M) and grain orientation spread (GOS) maps were constructed to show the angle distributions of intragranular misorientations and their averages within each grain. The misorientation axes were computed and plotted at pole figure and inverse pole figure to display the preferred orientations of intragranular misorientation axes in the specimen and crystallographic coordinates, respectively.

The above-mentioned microstructure parameters are useful when characterizing the mineral crystallographic and shape fabrics in a rock. In this study, the treatment and analysis of EBSD data were completed using the MTEX toolbox (ver. 5.2.beta2) in MATLAB (http://mtex-toolbox.github.io/) (Bachmann et al., 2010; Hielscher & Schaeben, 2008).

4.3. Whole-Rock and Mineral Compositions and P-T Calculation

The bulk-rock major oxides (SiO_2, Al_2O_3, TiO_2, total Fe_2O_3, CaO, MgO, K_2O, Na_2O, MnO, and P_2O_5) were measured on a fused glass disk made of whole-rock powder and lithium metaborate using an Axios^{max} X-ray fluorescence spectrometer at the Hebei Institute of Regional Geology and Mineral Resource Survey, China. Loss on ignition (LOI), bound or combined water (H_2O^+), and hydroscopic water (H_2O^-) were determined by placing 1 g of sample powder in the furnace at various temperatures (1000 °C for LOI and H_2O^+, 105–110 °C for H_2O^-) for several hours before being cooled in a desiccator and reweighed. The FeO content was measured using a routine wet dissolution-titration chemical method. The Fe_2O_3 content was calculated by subtracting FeO from the total Fe_2O_3 determined using X-ray fluorescence. The relative analytical uncertainties are <3% for most elements.

The major oxide compositions of the constituting minerals were analyzed using a wavelength-dispersive electron probe microanalyzer (JEOL JXA-8100) at Gyeongsang National University in Jinju, South Korea. The measurements were conducted using a 15 kV acceleration voltage, 10-nA beam current, 1-μm beam size, and 20-s counting time. The natural mineral standards were used for calibration and the final data were corrected using the atomic number (Z), absorption (A) and characteristic fluorescence (F) (ZAF) method.

The mineral formulae were calculated using the AX program developed by Prof. Tim Holland (https://www.esc.cam.ac.uk/research/research-groups/research-projects/tim-hollands-software-pages/ax).

To estimate the metamorphic P-T conditions of the eclogites, phase equilibria modeling was conducted using the Theriak/Domino software (09.03.2019) (de Capitani & Petrakakis, 2010) with the latest internally consistent data set (Database tcds62c) (Holland & Powell, 2011). The most recent activity models of the following minerals were used: garnet, orthopyroxene, biotite, chlorite, and ilmenite (White et al., 2014; White et al., 2014) and clinopyroxene, amphibole, and melt (Green et al., 2016). The relevant P-T pseudosections were constructed in the $MnO-Na_2O-CaO-K_2O-FeO-MgO-Al_2O_3-SiO_2-H_2O-TiO_2-O$ model system (MnNCKFMASHTO). To obtain more reliable peak P-T estimates for MEC and FEC, effective local bulk-rock compositions—which are calculated from the chemical compositions (from electron probe microanalyzer data) and volume proportions (from small-area EBSD phase maps) of the mineral assemblages that assured to be involved in the metamorphic reactions in a local domain—and intersections of pyrope and grossular isopleths of garnet were employed. Particularly, the effective bulk-rock water contents are estimated from the compositions and volume proportions of hydrous phases (amphibole and phlogopite) and they are obviously different between MEC and FEC. The effective bulk-rock composition data and their estimation details are shown in the caption of Figure 15. Besides, an independent thermobarometer relying on the mineral pairs of coexisting amphibole and plagioclase (Holland & Blundy, 1994; Molina et al., 2015) was also used to more tightly confined the retrograde P-T conditions where these two minerals are stable and which are not well constrained by phase equilibria modeling method.

4.4. Fourier Transformation Spectroscopy

To measure the hydrogen species and concentrations in the nominally anhydrous minerals (NAMs, e.g., Ol, Grt, Omp, and Opx) in eclogite, the unpolarized Fourier transformation infrared spectroscopy was used (Nicolet 6700 infrared spectrometer at the Tectonophysics Laboratory of Seoul National University in Korea). Doubly polished thin slices of the rock samples (~80–280 μm thick) were prepared in a routine process and dried at 120 °C in an oven for at least 24 hr before the infrared (IR) analysis. The IR absorption spectra were collected by averaging a series of 128 scans with a resolution of 4 cm^{-1}. During the measurement, dry and pure nitrogen gas was flushed into the system to reduce the disturbance caused by moisture in the air. Clean areas in the grains that were free of inclusions and cracks were selected for measurements. The size of the rectangular apertures (40–100 μm in length) varied with the shape and size of the clean regions in a grain.

5. Results

5.1. Microstructures

5.1.1. MEC

This type of eclogite is characterized by a coarse-grained granular texture. The minerals are nearly randomly oriented and the eclogite appears massive in the outcrop and hand specimen (Figure 3). The MEC mainly consists of olivine (Ol), garnet (Grt), omphacite (Omp), orthopyroxene (Opx), phlogopite (Phl), ilmenite (Ilm), amphibole (Amp), minor spinel (Sp), and plagioclase (Pl) (Figure 3). Olivine is a major phase and often occurs in different size (up to 2 mm) crystals with rhombic or prismatic shapes (Figure 3a). Almost all olivine crystals have coronitic rims, which are typically indicated by an inner rim of pure Opx and an outer rim that mainly consists of Omp edged with thin Pl layer in contact with neighboring Grt (Figure 3c). The Opx and Omp are polycrystalline and aligned in a palisade pattern with their long axes perpendicular to the Ol grain boundaries (Figure 4a). Ilmenite occurs sporadically in the matrix (~0.1–1 mm in length) and also displays coronitic rims. It is surrounded by an inner continuous Phl grain, which contains abundant Omp inclusions near its rim, and an outer Omp to Amp edge in contact with the neighboring Grt (Figure 3d). Most Ol grains show no obvious evidence for deformation by intracrystalline plasticity, such as undulose extinction and subgrain boundaries, except for a few grains that displayed both brittle (cracks filled by Opx) and ductile (undulose extinction) features (Figure 3f).

In contrast to the typical isometric morphology, Grt is mostly irregular in shape and interconnected to form the matrix surrounding the olivine grains (Figures 3a, 3b, and 4). In some domains, Grt displays columnar, tabular or prismatic shapes (Figure 3b). The Grt is rich in inclusions. It shows a complex intergrowth
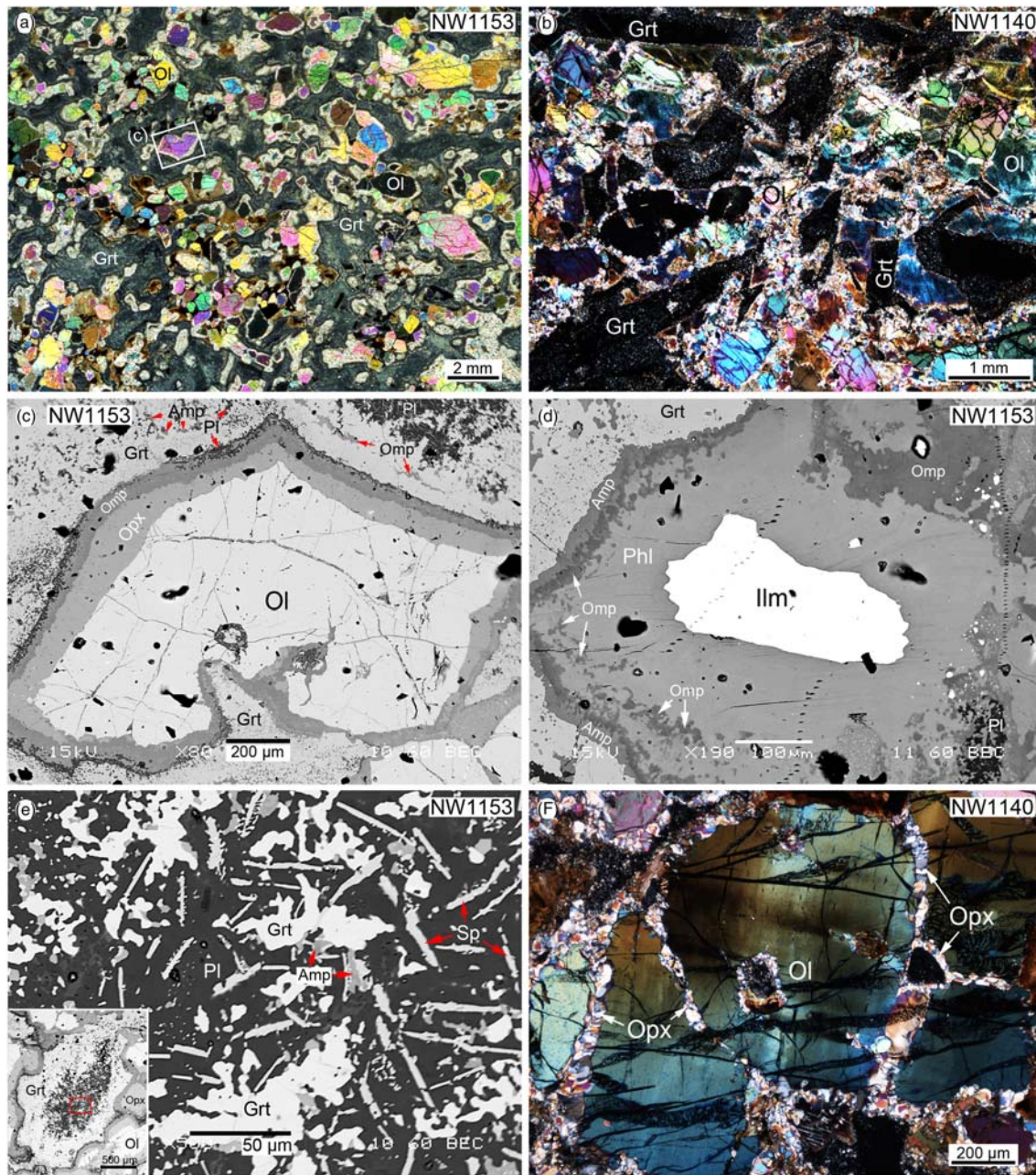
Figure 3. Optical photomicrographs (a, b, and f) and BSE images (c–e) showing the microstructures of MEC ($X'Y'$ plane). (a) Sample NW1153 displays variously sized and randomly orientated Ol crystals that have rhombic or prismatic shapes typical for euhedral Ol. Xenomorphic and inclusion-rich Grt constitutes the matrix surrounding Ol. (b) An enlarged view of Sample NW1140 with less xenomorphic Grt having columnar, tabular, or prismatic shapes. (c) A nearly rhombic-shaped Ol crystal (inset in (a)) showing coronitic reaction rims. This texture implies the prograde reactions: Ol + Pl → Opx + Grt and Opx + Pl → Omp + Grt. (d) A subhedral to anhedral Ilm crystal surrounded by a Phl crystal. This texture can be formed by the prograde reaction (Ol + Pl + Ilm + H_2O → Phl + Omp + Grt) or retrograde reaction (Omp + Ilm + H_2O → Phl) and retrograde reaction (Grt + Omp + H_2O ± Phl → Amp (calcic Amp)). (e) Pl-bearing inclusion-rich core in xenomorphic Grt (lower left inset). This texture denotes the prograde reaction: Ol + Pl + H_2O → Grt + Sp + Amp (calcic Amp). (f) A large and fragmented Ol crystal shows undulose extinction. The Ol-crosscutting fractures are filled with abundant fine-grained strain-free Opx crystals. Mineral abbreviation: olivine (Ol), garnet (Grt), orthopyroxene (Opx), omphacite (Omp), plagioclase (Pl), ilmenite (Ilm), phlogopite (Phl), spinel (Sp), and amphibole (Amp).

consisting of anhedral Grt, Pl, Amp, and needle-shaped Sp in the Pl-bearing core (Figure 3e), but contains mostly Omp and Amp inclusions in the mantle and rim regions (Figures 3c). Although Grt grain boundaries are hardly recognizable in both optical and backscattered electron images, they are
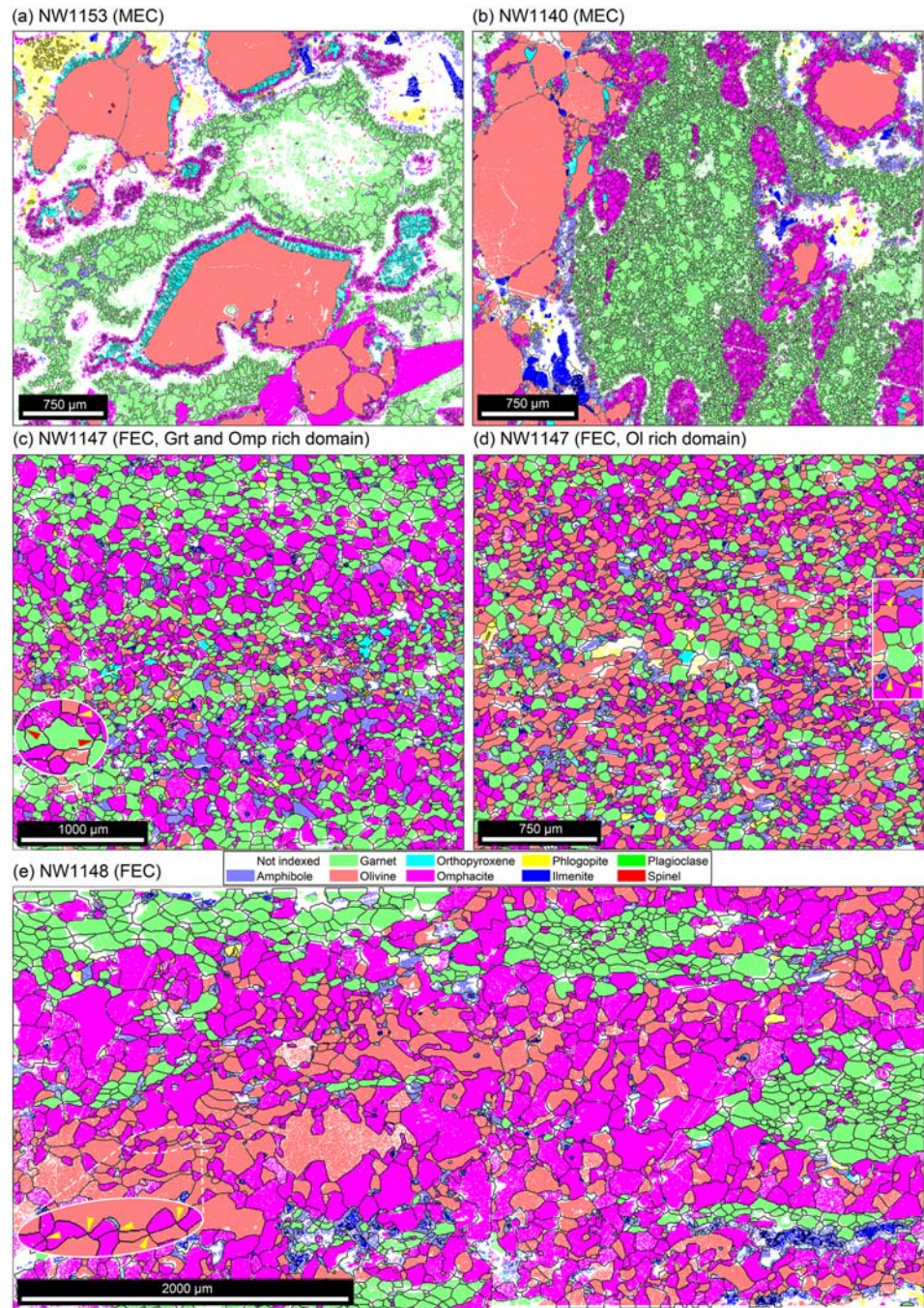
Figure 4. EBSD phase maps of (a and b) MEC and (c–e) FEC samples showing the spatial distributions of mineral phases and the grains boundaries, which are marked as black lines. Colored arrows in the insets (oval and rectangular areas in c–e) highlight the presence of four (occasionally five) grain junctions.

ubiquitously observed in the EBSD phase maps when misorientation angles larger than 10° are set to define grain boundaries (Figures 4a and 4b). These observations imply that the large and irregularly shaped Grt is actually fine-grained polycrystalline aggregate which seemingly has grain sizes increased from the rim toward core regions (Figure 4a and 4b). Alternatively, many small "grains" in the Grt could be subgrains if the minimum misorientation angle required to form a grain boundary in Grt crystal is greater than 10°. The Grt in MEC thus consists of either numerous small grains or subgrains.

5.1.2. FEC

The FEC is intensely deformed and shows distinct foliation and lineation in the outcrop and hand specimen. In XZ plane thin sections, the foliation is well defined by the mineral layering. The mineral assemblage of FEC is Grt + Omp + Ol + Amp + Phl + Opx + Ilm + minor Pl and Sp, which is the same as that of MEC. Based on the grain size and degree of foliation development, we identified two FEC subtypes. Subtype-I (NW1142, NW1143, NW1144, and NW1148) shows prominent foliation, which is featured by the layering of fine-grained mineral mixtures and by large elongated foliation-parallel Grt bands (Figure 5a). Subtype-II (NW1147) is more intensely foliated and displays layers of finer grained mixtures of minerals and more elongated parallel-aligned Grt-rich bands (Figure 5b).

The grain sizes are much smaller in Subtype-II ($d_{avg.}$ ~ 50–130 μm) than those in the Subtype-I ($d_{avg.}$ ~ 100–230 μm) for all major phases (Omp, Grt, Ol, Opx, and Amp) and their composites (all phases) (Figures 6b and 6d). A few domains in Subtype-I show much larger grain size of Ol (d_{Ol} > 300 μm) due to the presence of Ol porphyroclasts (Figures 5a and 5c). In both subtypes, the minerals of major phases and their composites mostly have small aspect ratios ($R < 2$) which are overall lower in Subtype-II than Subtype-I, especially for Omp, Grt, and Ol (Figures 6a, 6b, 7b, 7d, and 7f). Despite the relatively vague SPOs of minerals observed in the optical images (Figures 5c and 5d) and EBSD phase maps (4c–e), the statistics show obvious SPOs of the long axes of all major phases (especially Grt, Ol and Omp) that align subparallel to the foliation in both subtypes (Figures 7a, 7c, and 7e and Figure S1 in the supporting informarion). However, the major phases also exhibit minor differences in the SPOs as indicated by their different angles to the foliation (Figures 7a, 7c, 7e, and S1). A combination of aspect ratio and SPO suggests that the larger the aspect ratio of a grain (of all major phases), the smaller angle of the long axes to foliation tends to develop (Figures 7b, 7d, and 7f).

In both subtypes, the grains are mostly equigranular and have straight boundaries (Figures 4c–4e, 5c, and 5d), which is also proven by the small shape factors in all major phases (Figures 6a and 6c). The shape factor varies in the range of ~1.2–1.7 and it is the highest and lowest in Opx (~1.48–1.66) and Grt (~1.18–1.24), respectively. The Subtype-II has overall smaller shape factors than Subtype-I, especially for Omp, Grt and Ol. Additionally, the shape factor tends to increase with both aspect ratio (Figure 6a) and GOS (Figure 6c), whereas the tendencies are relatively weaker between grain size and aspect ratio (Figure 6b) or GOS (Figure 6d).

In Subtype-I, large and lenticular Ol porphyroclasts frequently occur in the matrix between Grt bands (Figures 5a and 5e). These Ol porphyroclasts display ambiguous undulose extinction or subgrain boundaries in the optical images, which are more readily accessed in the M2M orientations maps (see section below). The grain boundaries of Ol porphyroclasts are mostly curved to irregular and embayed or "engulfed" by small Opx and Omp crystals (Figures 4e and 5e). Polygonal hydrous silicate patches (e.g., Phl and Amp) and occasionally minute needle-shaped inclusions are common features in Ol porphyroclasts (Figure 5e). The Grt bands or pockets in both subtypes consist of mainly polygonal shaped Grt grains, which are often locally mixed with other phases, mainly Omp and Amp and less Ol and Phl (Figures 4c–4e). In an Ol-rich domain of Subtype-II, Grt grains are more dispersed and well mixed with other major phases such as Omp, Ol, and Amp (Figure 4d). The major constituent phases are actually well mixed in both subtypes, although the mixing seems more intensive in Subtype-II than Subtype-I (cf. Figure 4c, 4d, and 4f). Besides the prevalence of 120° triple junctions that are formed by the same or different phases, four or even five grain junctions are also frequently observed but are more common among different phases (e.g., Omp-Grt, Omp-Ol, and Omp-Ol-Amp junctions) (see insets in Figures 4c–4e)

An amoeboid symplectite complex frequently occurs in the matrix, which is commonly characterized by an irregular Omp grain surrounded by vermicular anhydrous Opx, Ab and neighboring hydrous Amp (Figure 5f). Corona textures of Phl around Ilm and Amp around Phl are also frequently observed in the matrix (Figures 5c and 5d).

5.2. Crystallographic Fabrics
5.2.1. CPOs of Minerals

In the MEC, the [001] axes of Ol are aligned subparallel to the apparent lineation (X'), while the maxima of the [010] axes are at high angle (~45°) to the apparent foliation ($X'Y'$) and [100] axes are rather dispersed (Figures 8a and 8b). This CPO pattern resembles the B-type CPO if the $X'Y'$ plane is approximating the
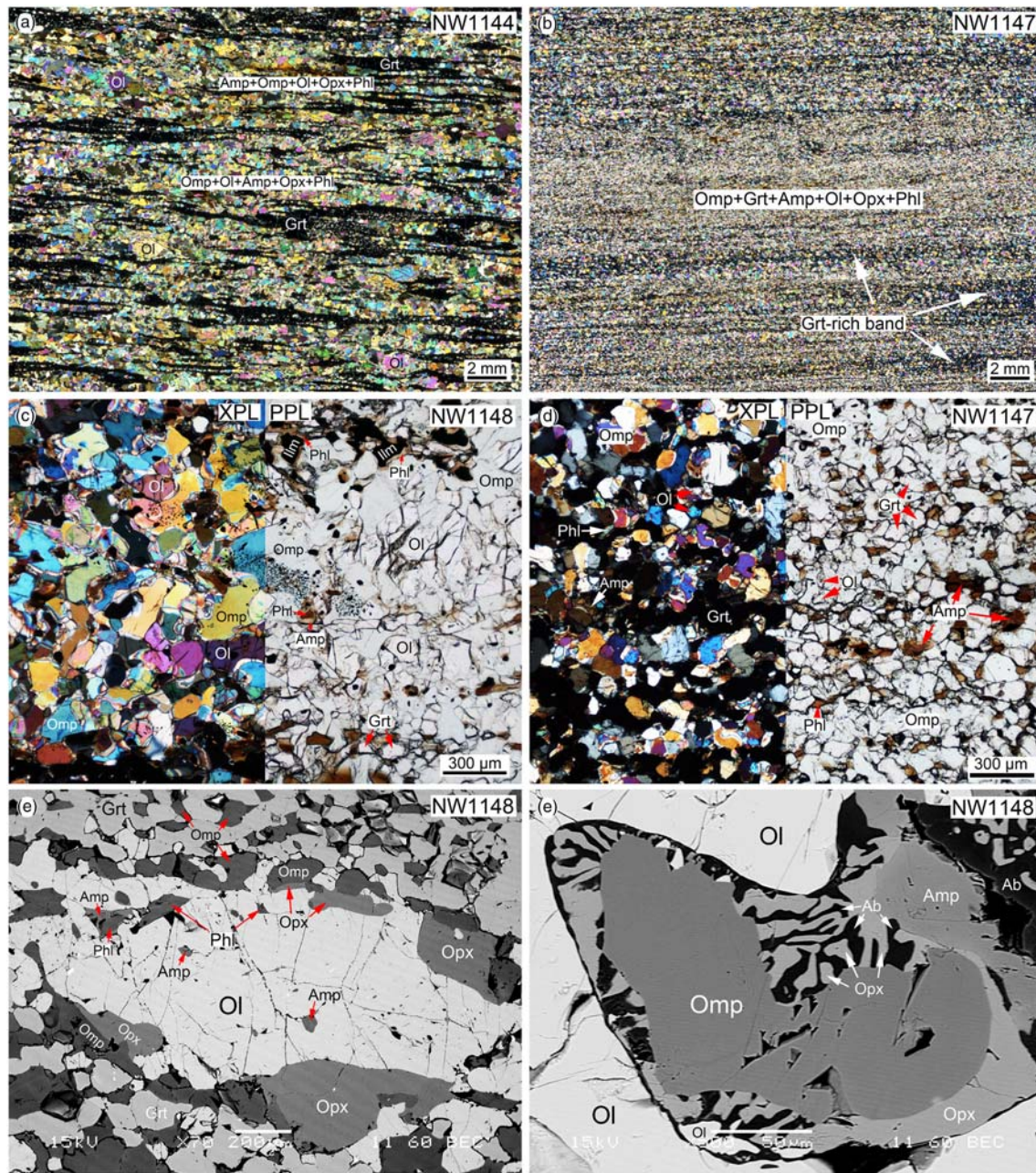
Figure 5. Optical photomicrographs (a–d) and BSE images (e and f) showing the microstructures of FEC (*XZ* plane). (a) Sample NW1144 shows a distinct foliation. Large Ol porphyroclasts notably occur in the fine-grained matrix. (b) Sample NW1147 displays a more intense foliation. (c) Enlarged view showing a matrix domain in Sample NW1148 presenting textures similar to Sample NW1144 (a). The Phl corona around Ilm and Amp corona around Phl are shown, indicating the prograde or early retrograde reactions: Omp + Ilm + H_2O → Phl and Omp + Phl + H_2O → Amp (sodic-calcic Amp). (d) Enlarged view of a matrix domain in Sample NW1147. The left and right images of (c) and (d) were taken under cross- and plane-polarized light, respectively. (e) Texture of a large lens-shaped Ol porphyroclast in Sample NW1148, implying the prograde reaction: Ol + Pl → Opx + Grt + Omp. (f) Amoeboid symplectite complex in Ol, suggesting the late retrograde reaction: Omp + H_2O → Opx + Pl + Amp (calcic Amp).

real foliation of MEC. In the FEC, the CPOs of Ol are rather variable and lack of systematic pattern. Overall, the maximum of [010] axes tend to align at the plane perpendicular to lineation (*YZ* plane) (Figures 8d–8g), while either or both [100] and [001] axes cluster subparallel to *X* or *Y* axes (Figures 8c and 8e–8g). Based on the CPO patterns of Ol, we identified A-type like and [010]-axial or AG-type like CPOs of Ol for the Subtype-I samples of NW1148 (Figure 8g) and NW1143 and NW1144 (Figures 8d and 8e), respectively. The Subtype-I
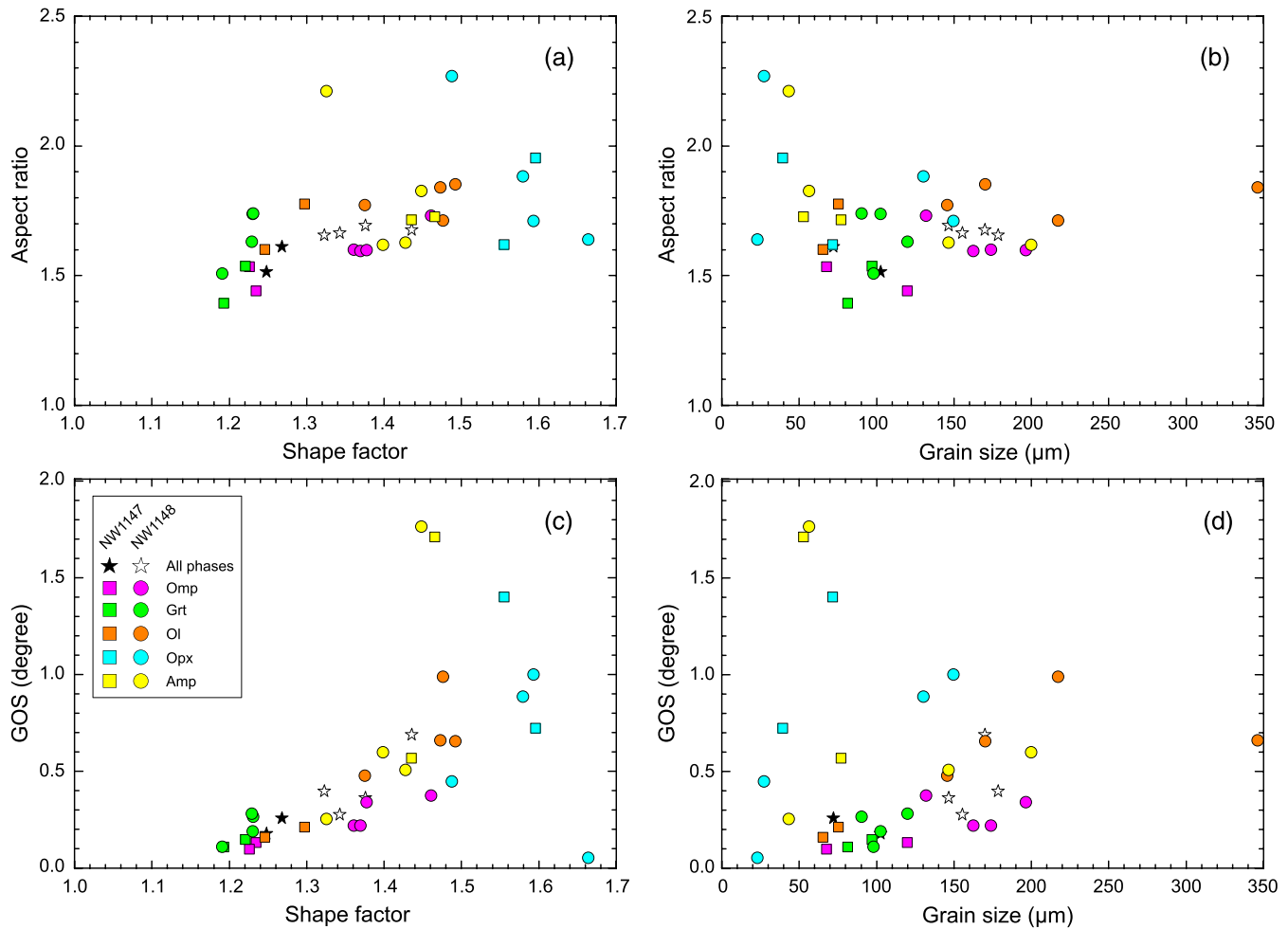
Figure 6. Diagrams showing the relationships of aspect ratio versus shape factor (a) and grain size (b), as well as of GOS versus shape factor (c) and grain size (d) in several domains from two FEC subtypes (NW1147 and NW1148). All values are weighted arithmetic means by grain areas.

sample of NW1142 and Subtype-II sample of NW1147 presented CPOs (Figures 8c and 8f) that cannot be categorized into the current classification of olivine CPO types (Jung, 2017).

In the MEC, the [001] axes of Opx are also concentrated at high angles (~45°) to *X′Y′ p*lane, whereas the [100] and [010] axes are less clustered (Figures 8a and 8b). Notably, the MEC Sample NW1153 displays two clear maxima of [100] and [010] axes at low angles to *X′Y′ p*lane. In the FEC, except for the Subtype-I Sample NW1148 and Subtype-II Sample NW1147 that display Opx [001] axes at high angle to lineation and fairly dispersed [100] and [010] axes (Figures 8f and 8g), the other three Subtype-I samples have pronounced concentrations of Opx [001] axes and weak girdles of [010] axes aligning parallel and perpendicular to the lineation, respectively (Figures 8c–8e). The [100] axes are also quite scattered, but they are clustered parallel to lineation and perpendicular to foliation in the samples of NW1142 and NW1143, respectively (Figures 8c and 8d).

The CPOs of Grt in the MEC are characterized by the clustering of <100> axes in an orthogonal pattern and relatively more dispersed distributions of <111> and <110> axes (Figures 8a and 8b). In contrast, the <100> axes show several maximum at moderate angles (~45°) to foliation, while the <111> and <110> axes are similarly scattered and lack of consistent CPOs in all FEC samples (Figures 8c–8g). The CPO patterns of Grt are not completely random but present no apparent systematic distributions in both MEC and FEC.

Similar to Grt, Omp also develops obvious CPOs in the MEC as represented by the maximum of the [001] axes and (010) poles aligning at high angles to *X′Y′ p*lane while [100] axes are clustered subparallel to *X′Y*
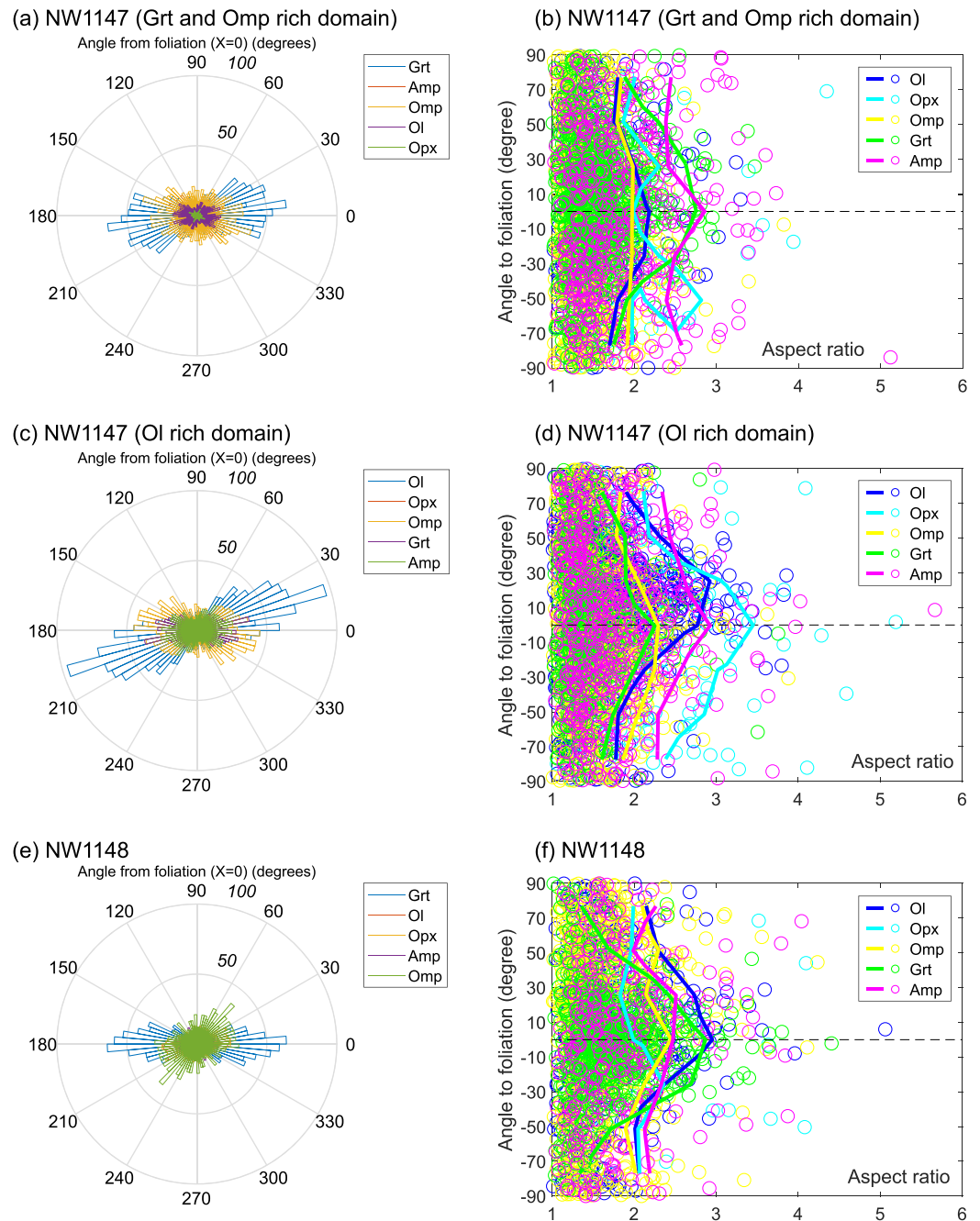
Figure 7. Rose diagrams (a, c, and e) showing the SPOs of the long axes of the major phases and *R-θ* diagrams (b, d, and f) displaying the relationships between aspect ratio and angle of long axes to the foliation for two FEC subtypes (NW1147 (a–d) and NW1148 (e and f)). Thick solid lines in (b), (d), and (f) are contours of 2% number density for each mineral.

′ *p*lane (Figures 9a and 9b). The CPOs of Omp in both subtypes of FEC are mainly characterized by [001] axes subparallel to the lineation and [100] axes, (110) and (010) poles (with (010) pole maximum aligning subnormal to the foliation) forming weak girdles subperpendicular to the lineation (Figures 9c–9g). Differing with other FEC samples, Subtype-I NW1142 displays maximum of [100] axes subparallel to lineation (Figure 9c).

The CPOs of Amp are well correlated with those of Omp in the MEC, as reflected by the coincidental alignments of [001] axes, (010) poles and [100] axes or poles between Amp and Omp (Figures 9a and 9b). In FEC,
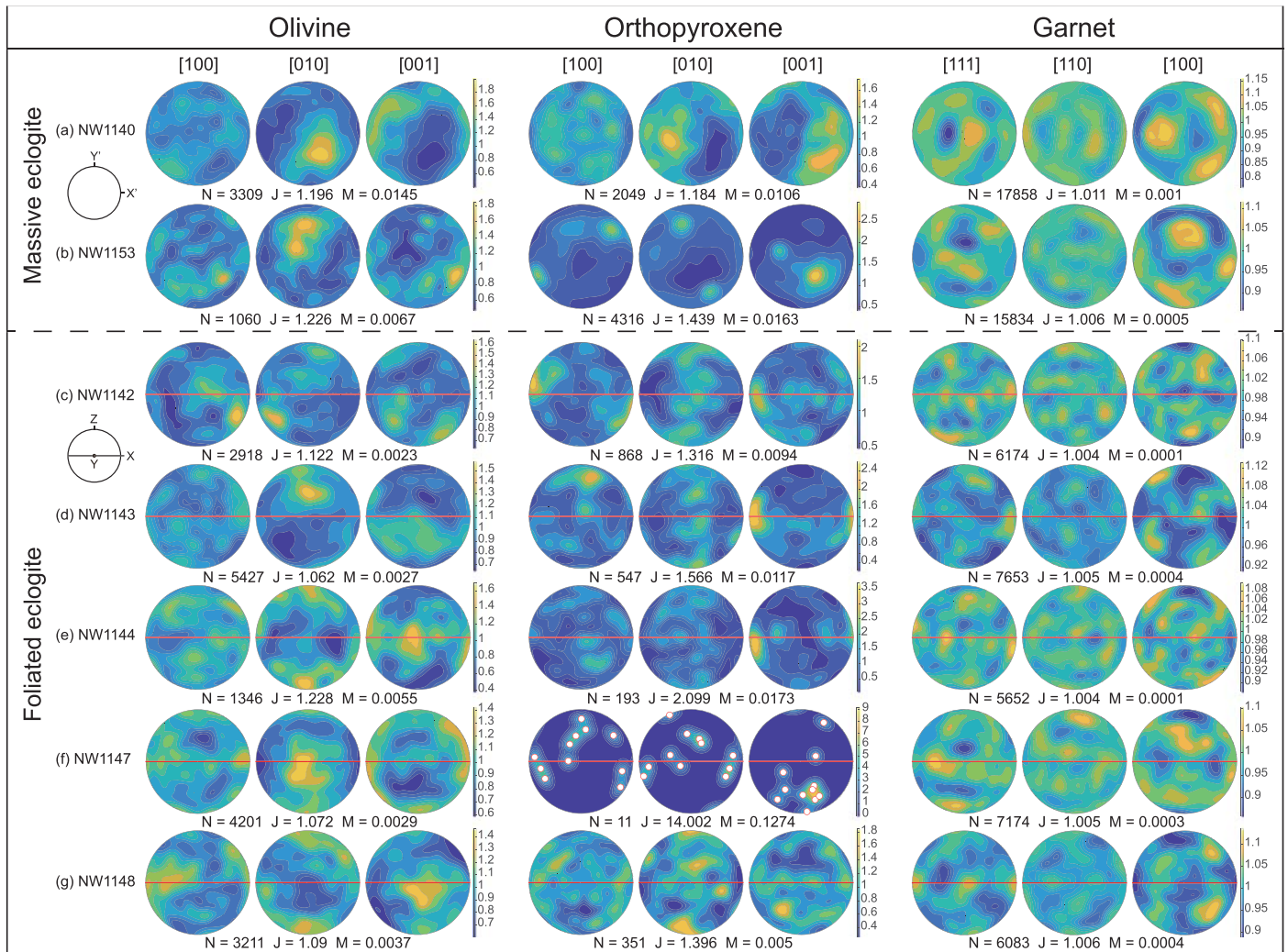
Figure 8. CPOs of Ol (left column), Opx (middle column), and Grt (right column) in (a, b) MEC and (c–g) FEC. Pole figures are presented in an equal area, lower hemisphere and contoured with a resolution of 1°. X, Y, and Z denote the lineation, direction perpendicular to the lineation and parallel to the foliation, and foliation-normal direction, respectively. Superimposed circles in (f) are scattered orientations of Opx grains. X′ and Y′ are the apparent lineation and the direction perpendicular to the lineation on the apparent foliation (X′Y′ plane). N: number of grains, M: M-index, and J: J-index.

except for one Subtype-I Sample NW1148, which develops rather weak Amp CPO (Figure 9g), all other Subtype-I samples present a CPO featured by [001] axes aligning parallel to lineation and both poles of (100) and (110) concentrating perpendicular to foliation (Figures 9c–9e). The Subtype-II Sample NW1147 present an Amp CPO showing the alignment of [001] axes parallel to lineation, but poles of (010) and (100) clustering to respective Z and Y axes (Figure 9f).

5.2.2. CPO Strength

Except that one Subtype-II Sample NW1147 has a large CPO strength of Opx due to its limited number of grains (Figure 8f) and one Subtype-I Sample NW1143 has a strong CPO strength of Amp (Figure 9d), the CPOs of major constituent minerals (Omp, Grt, Ol, Opx, and Amp) in both MEC and FEC develop J- and M-index smaller than 2.5 and 0.06, respectively (Figures 8, 9, and S2). Overall, the CPO strength of the minerals increases in the order of Grt < Ol < Omp < Amp ~ Opx (Figure S2). Besides, neither J-index nor M-index vary considerably with grain size in the FEC (Figure 10).

5.2.3. Misorientations

The intragranular misorientation angles (0–10°) distribute rather heterogeneously in the FEC and they are less than 1° in most grains (Figure 11). In the Subtype-II Sample NW1147, the misorientation angles larger
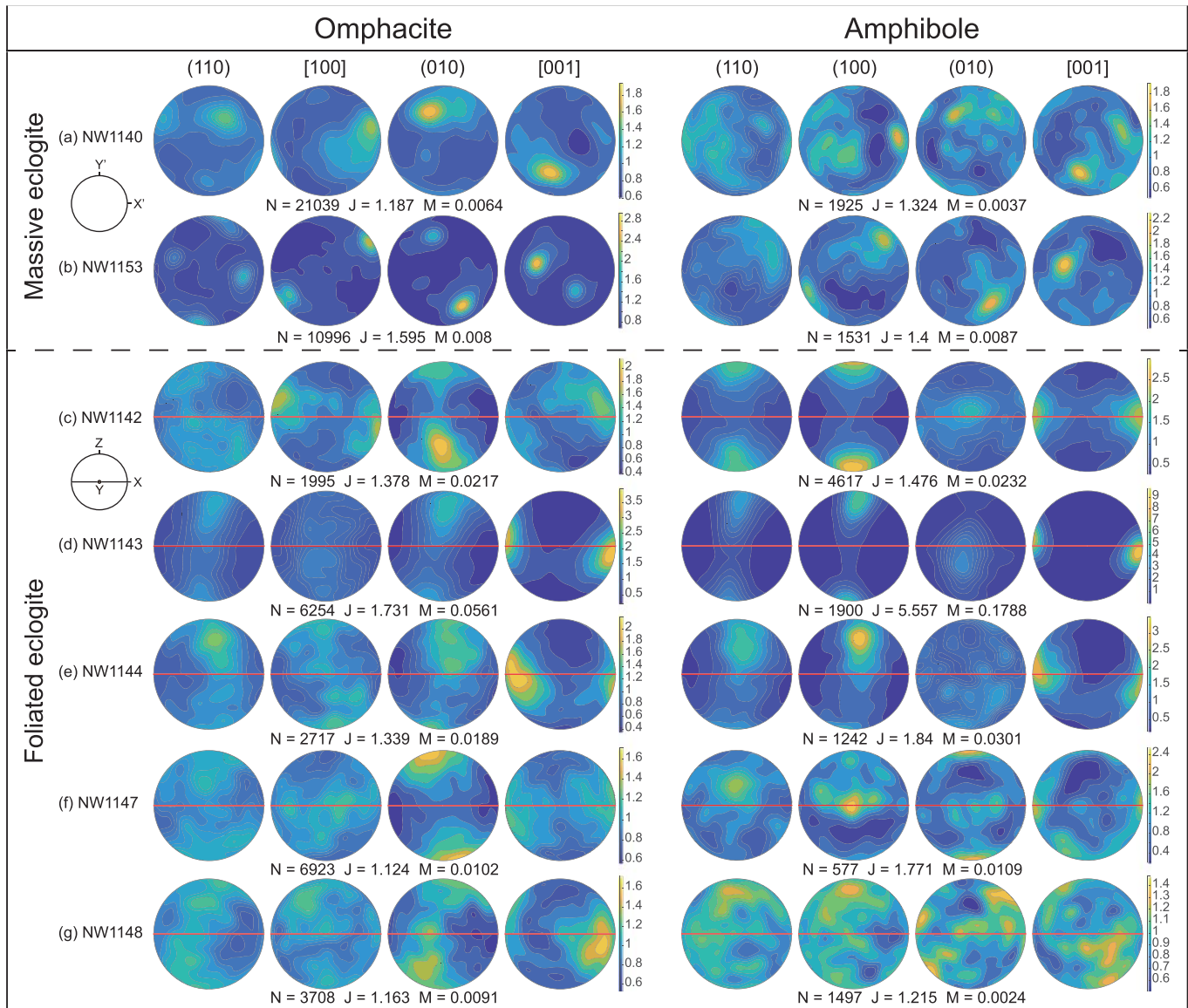
Figure 9. CPOs of Omp (left column) and Amp (right column) in (a, b) MEC and (c–g) FEC. Reference frame and descriptions on the pole figure are the same as those in Figure 8.

than 2° are mostly found in Opx and Amp (Figures S3 and S4), whereas Ol and Amp develop greater misorientation angles (>2°) than Grt, Omp and Opx in the Subtype-I NW1148 (Figure S5). Similar results are also reflected by the GOS values in which Amp, Opx and Ol have overall larger GOS (>0.5°) than the Grt and Omp (<0.5°) (Figures 6c and 6d). Besides, Subtype-II Sample NW1147 shows obviously lower GOS values in Grt, Omp and Ol than Subtype-I Sample NW1148 (Figures 6c and 6d).

The intragranular misorientation axes (2–10°) in the major constituent minerals (Omp, Grt, Ol, Opx, and Amp) in two subtypes of FEC are nearly randomly distributed in the specimen coordinates (Figures S6–S8). Different from other phases that have variable clustering directions of misorientation axes in the crystal coordinates, Ol mostly has the misorientation axes aligning parallel mainly to the [010] axis and secondarily to the [100] and [010] axes (Figures S6a–S8a). The CPOs of the grains that develop intragranular misorientation angles of 2–10° are often not in good consistencies with the CPOs of the complete grain data set, which contains the grains of both large (2–10°) and small (<2°) intragranular misorientation angles (cf. left and middle columns in Figures S6–S8).
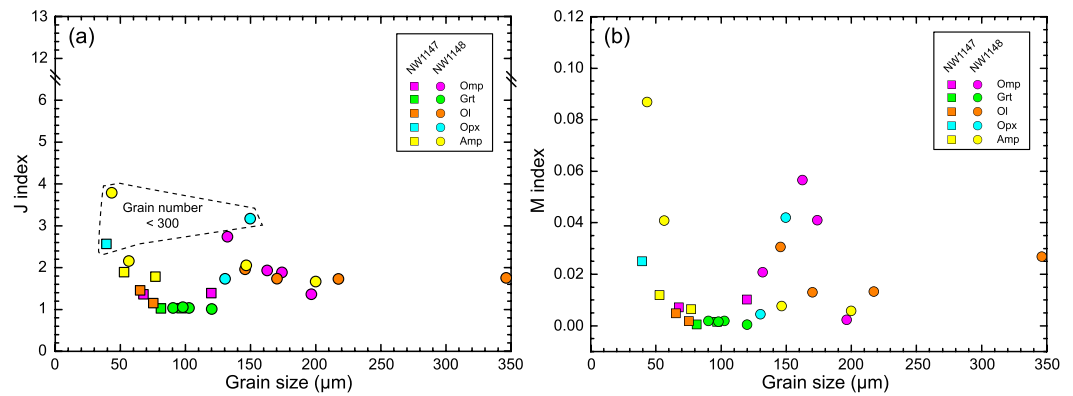
Figure 10. Diagrams showing the relationships between grain size and J-index (a) and M-index (b) derived from two FEC subtypes (NW1147 and NW1148). The data points whose elevated CPO strengths are mainly attributed to their limited numbers of grain are bracketed by the dashed line and should be excluded for the comparison of CPO strength between samples.

5.3. Whole-Rock and Modal Compositions

The bulk-rock major oxide concentrations vary in similar ranges for both MEC and FEC (Table 1). The low SiO_2 (~42–43 wt.%), $Na_2O + K_2O$ (~2.3–2.7 wt.%), Al_2O_3 (~10–13 wt.%), and CaO (~4.8–6.1 wt.%) and high $FeO + Fe_2O_3$ (~17–19 wt.%) and MgO (~16–19 wt.%) contents indicate the protoliths of eclogites are of mafic-ultramafic (picrite basalt) compositions. Notably, the LOIs are obviously lower in the MEC (0.67–0.83 wt.%) than those in the FEC (1.02–1.43 wt.%). The modal compositions (viz. volume proportions) were estimated based on the area fractions of phases on the large-area EBSD maps. Overall, the FEC contains less Ol but more Grt, Omp and Amp than MEC (Table 2).

5.4. Mineral Compositions of Major Elements
5.4.1. Garnet

In the MEC Sample NW1153, the compositional zoning of Grt shows fluctuations in pyrope (Prp), grossular (Grs) and almandine (Alm), but nearly flat spessartine (Spss) components in an off-center "core" region, and overall homogenous components in the mantle-rim regions (Figure 12a). Besides, the Pl-bearing Grt core exhibits significantly higher Grs and lower Prp proportions than the Pl-free regions (Figures 12c and 12d). The MEC Sample NW1140 has no Pl-bearing core and shows relatively higher Prp and lower Grs contents (Figures 11c and 11d). In contrast, FEC Subtype-II Sample NW1147 displays no compositional zoning, which is characterized by nearly flat Alm, Prp, Grs, and Spss patterns in Grt (Figure 12b). Overall, FEC shows lower Grs and higher Prp contents than MEC (Figure 12). Excluding the Pl-bearing region, MEC shows a negative correlation between Grs and Prp (Figure 12c) and a positive correlation between Prp and Alm (Figure 12d). These correlations are also manifested in the Grt compositional profile of MEC in which Alm and Prp show roughly concordant variations, whereas Grs and Prp display opposite fluctuations (Figure 12a). In contrast, FEC exhibits a weak anticorrelation between Grs and Prp (Figure 12c) but a distinct negative correlation between Prp and Alm (Figure 12d). This negative correlation can also be observed in the Grt compositional profile of FEC in which Prp and Alm present opposite patterns (Figure 12b).

5.4.2. Clinopyroxene/Omphacite

The Omp in the FEC has averagely higher Ae contents compared to the MEC (Figure S9a). The Na content and $Fe_t/(Fe_t + Mg)$ ratio of the Omp in the FEC overlap with those of the MEC but are averagely higher (Figure S9b). The Omp shows no remarkably different compositions between the inclusions in Grt or Ol and the coronitic rims around Ol or Ilm in the MEC, as well as between the core and rim in the FEC.

5.4.3. Olivine and Orthopyroxene

The Mg# [$=100 \times Mg/(Mg + Fe^{2+})$] of Ol varies slightly from 66 to 70 in the MEC and FEC (Figure S10a). Excluding three outliers, the Mg# and NiO content (~0.08–0.20 wt.%) present an overall positive intersample correlation (Figure S10c, magmatic origin). Including outliers, weak negative intrasample correlations between the Mg# and NiO content are displayed in the FEC Samples NW1147 and NW1148 (Figure S10c, metamorphic origin). No significant differences in the Ol compositions are observed between the core and
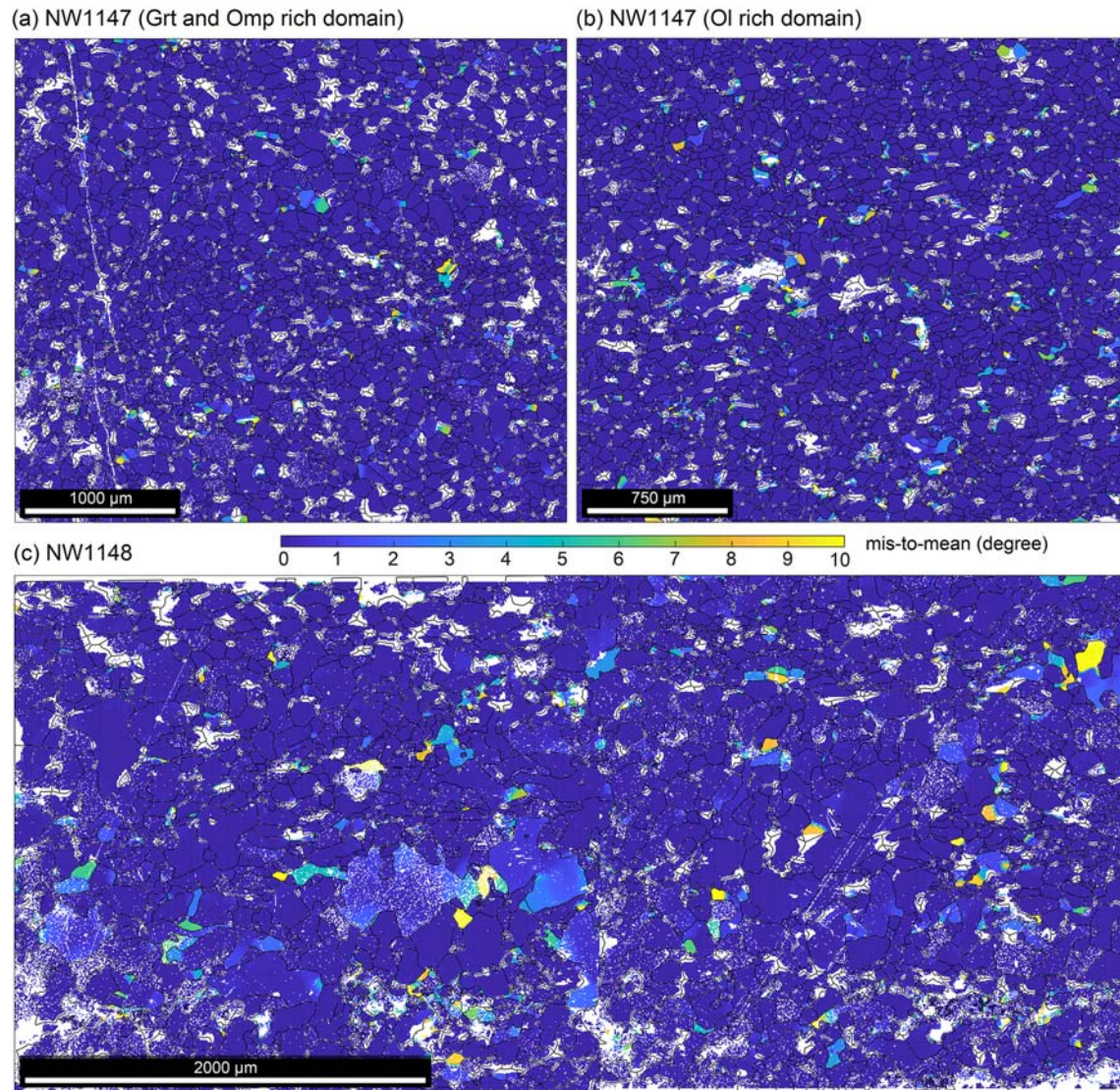
(a) NW1147 (Grt and Omp rich domain)

(b) NW1147 (OI rich domain)

(c) NW1148

mis-to-mean (degree)

Figure 11. (a–c) Mis-to-mean (M2M) orientation maps showing the intragranular misorientation angle distributions (0–10°) of all constituent phases in two FEC subtypes samples.

rim areas or between the porphyroclast and matrix grains. The Opx Mg# also varies slightly (~72.5–76) and exhibits no remarkable differences between MEC and FEC (Figure S10b). The Opx compositions are dominated by enstatite and ferrosilite component (Figure S10d). The Al_2O_3 content of Opx (~0.24–0.36 wt. %) is very low in both MEC and FEC.

5.4.4. Amphibole and Mica

The compositions of Amp are mainly calcic and sodic-calcic in the MEC and FEC, respectively (Figure 13a). The calcic Amp in both MEC and FEC is pargasite (Figure S11a), whereas the solid-calcic Amp is Mg-katophorite in the FEC and Mg-taramite in the MEC (Figure S11b). The calcic Amp in the FEC occurs only in the symplectite complex (Figure 5f). The Fe/(Fe + Mg) ratio and average Si molar ratio of mica fall into a composition of Phl in both MEC and FEC (Figure 13b).

5.4.5. Feldspar, Ilmenite, and Spinel

The feldspar compositionally belongs to oligoclase in both MEC and FEC (Figure S12). The Ilm has high FeO (~42–45 wt.%) and TiO_2 (~50–53 wt.%) and low MgO (~2.1–3.8 wt.%) and MnO (~0.15–0.28 wt.%) contents in both MEC and FEC. The Sp occurring in the Pl-bearing Grt core in the MEC presents high Al_2O_3 (~59–61 wt. %) and FeO (~25–26 wt.%), and low MgO (~11–12 wt.%) and NiO (~0.14–0.20 wt.%) contents.

Table 1
Measured Bulk-Rock Major Element Compositions (wt.%)

Sample	Rock type	SiO_2	Al_2O_3	TiO_2	Fe_2O_3	FeO	CaO	MgO	K_2O	Na_2O	MnO	P_2O_5	LOI	Total
NW1140	MEC	42.05	10.18	0.96	1.77	17.62	4.83	19.13	0.47	1.78	0.24	0.16	0.67	99.85
NW1153	MEC	42.90	12.27	1.06	1.42	16.22	5.82	16.46	0.59	1.90	0.22	0.19	0.83	99.88
NW1144	FEC	43.10	12.08	0.99	2.19	14.95	6.10	16.35	0.43	2.10	0.20	0.17	1.18	99.85
NW1147	FEC	43.42	12.79	0.91	2.32	14.62	6.03	15.69	0.50	2.18	0.22	0.16	1.02	99.86
NW1148	FEC	41.96	10.34	0.92	1.63	17.35	5.07	18.47	0.47	1.81	0.24	0.15	1.43	99.85

Note. LOI: loss on ignition.

5.4.6. Hydrogen Concentrations in NAMs

Despite the interference of noise (peaks occurring consistently at the same wavenumbers in all studied samples) above 3,600 cm^{-1} which is the main IR absorption range of hydrous silicates, all single crystalline NAMs (Grt, Ol, Omp, and Opx) in the MEC and FEC present fairly flat IR spectra below 3,600 cm^{-1}, which commonly indicates the absorption of hydrogen impurities in the crystal lattice of NAMs (Figure 14). Because of the absence of prominent absorption bands of hydrogen below 3,600 cm^{-1}, the exact water content of the specimen was not calculated and considered to be trivial.

5.5. Metamorphic P-T Conditions and Paths

Disparate peak metamorphic P-T conditions are inferred for two representative MEC (NW1153) and FEC (NW1147) samples. Excluding the data at higher temperature end—which have large uncertainties due to the poor convergences of subparallel-aligned isopleths of Grs and Prp—Grt compositions in the mantle-to-rim region yield peak P-T conditions of ~1.0–2.5 GPa and ~600–750 °C for MEC (Figure 15a). In contrast, eliminating three outliers at the lower pressure end (the same reason as above), the Grt compositions in the FEC suggest peak metamorphic conditions at P ~ 2.7–3.7 GPa and T ~ 700–820 °C (Figure 15b). The fact that peak P-T conditions are higher in the FEC than MEC is reflected by the higher Prp and lower Grs contents in the Grt as well as the higher Na contents in Omp and Amp in the FEC than those in the MEC (Figures 12, S9b, and 13a). The peak P-T results for FEC suggest that Flem eclogites experienced UHP metamorphism during prograde (i.e., subduction or burial) and/or early retrograde (i.e., early exhumation) stages, which are consistent with the inference for the Nordøyane UHP domain where Flem eclogites occur (Hacker et al., 2010). Besides, the metamorphic P-T conditions for the symplectite assemblages of Amp-Pl-Opx in the FEC and Amp-Pl-Phl in the MEC are similar and estimated to be ~0.8–1.0 GPa & ~710–760 °C and ~1.2 GPa and 700 °C, respectively (yellow rectangle and star in Figure 15), representing a late retrograde (i.e., late exhumation) event.

6. Discussion and Implications

6.1. Deformation Enhanced Eclogite-Facies Metamorphism

As shown above, the peak P-T metamorphic conditions of weakly deformed MEC (~1.0–2.5 GPa and ~600–750 °C) and strongly deformed FEC (~2.7–3.7 GPa and ~700–820 °C) display a significant gap. This result is contradictory to the observation that MEC and FEC (having almost the same bulk-rock compositions, Table 1) coexist in a single block (Figure 2), which implies that they should have experienced the same

Table 2
Normalized Phase Volume Proportions (vol.%) Based on the Area Fractions of Minerals on the Large-Area EBSD Maps

| Sample	Rock type	Grt	Omp	Ol	Opx	Amp	Phl	Ilm	Pl	Sp
NW1140	MEC	21.64	29.37	40.12	2.78	2.97	1.29	1.40	0.40	0.03
NW1153	MEC	24.41	21.10	40.68	6.39	2.73	1.19	2.11	1.03	0.34
NW1142	FEC	30.55	13.25	16.03	4.37	33.28	1.15	0.98	0.37	0.02
NW1143	FEC	22.95	30.03	30.00	2.63	12.05	1.00	0.82	0.50	0.02
NW1144	FEC	31.82	26.42	21.06	2.10	16.47	1.00	0.93	0.17	0.02
NW1147	FEC	36.56	38.29	18.45	0.36	4.71	0.88	0.55	0.19	0.03
NW1148	FEC	29.79	24.25	27.74	2.71	11.99	2.25	0.77	0.46	0.04
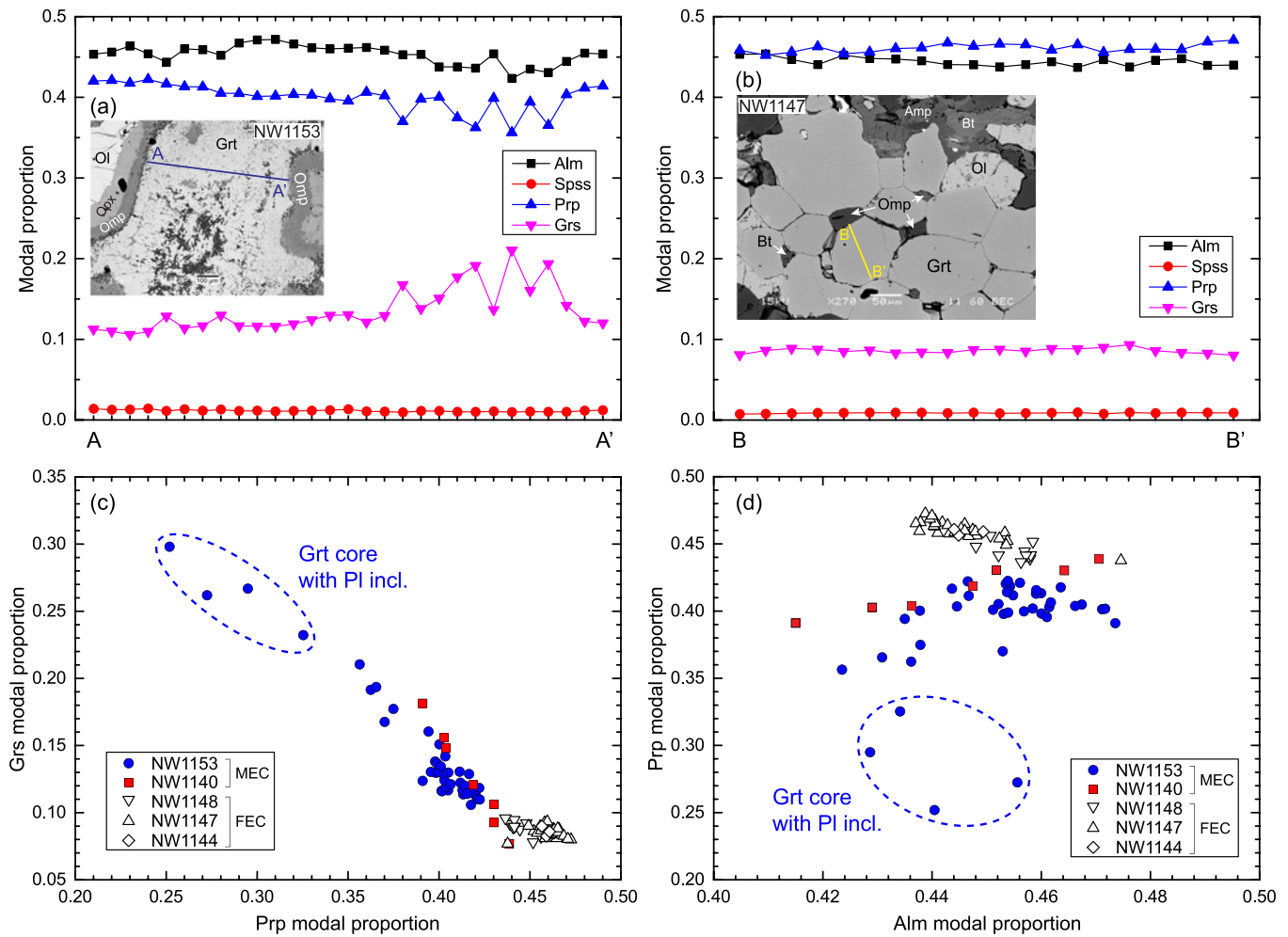
Figure 12. Compositions of garnet. (a) Compositional profile showing the variations of major Grt end-members along a solid blue line (A-A′ in the inset, excluding the dark Pl-rich core) of a Grt grain in MEC (NW1153). (b) Compositional profile showing the variations of major Grt end-members along a solid yellow line (B-B′ in inset) of a Grt grain in FEC (NW1147). (c) Grs versus Prp and (d) Prp versus Alm diagrams. The blue dashed ellipse marks the composition range of the Pl-bearing Grt core (NW1153).

P-T trajectory. Based on these facts, we infer that the deformation has mainly occurred at prograde and/or early retrograde stages, and it must play a crucial role in promoting the HP to UHP metamorphic transition (see also Mørk (1985)).

The water contents in the MEC and FEC also differ. Because major NAMs (Ol, Opx, Omp, and Grt) contain little hydrogen as indicated by their fairly flat IR spectra (Figure 14), water is almost completely stored in the hydrous phases in both MEC and FEC. The absence of free H_2O phase in most domains of the P-T pseudo-sections (Figure 15) also implies that, despite small in total quantity, almost all water resides in the hydrous silicates and little water can be absorbed by NAMs due to an extremely low water fugacity in the system. Despite the presence of free H_2O at the peak P-T condition in FEC (Figure 15b), its estimated concentration—avg. ~150 wt. ppm at the average P-T condition inferred from the plots of Grt composition in the Grt + Amp + Omp + H_2O assemblage and at the bulk-rock composition that includes unreacted olivine —is probably too low to hydrate the NAMs significantly (for a comparison, NAMs in natural eclogite predominantly have total H_2O content >200 wt. ppm; Katayama et al., 2006; Sheng et al., 2007; Wu et al., 2008). Therefore, the smaller LOI and volume proportions of hydrous minerals (Amp and Phl) in the MEC suggest that MEC is less hydrated than FEC (Tables 1 and 2). Besides, the water content at the peak metamorphic
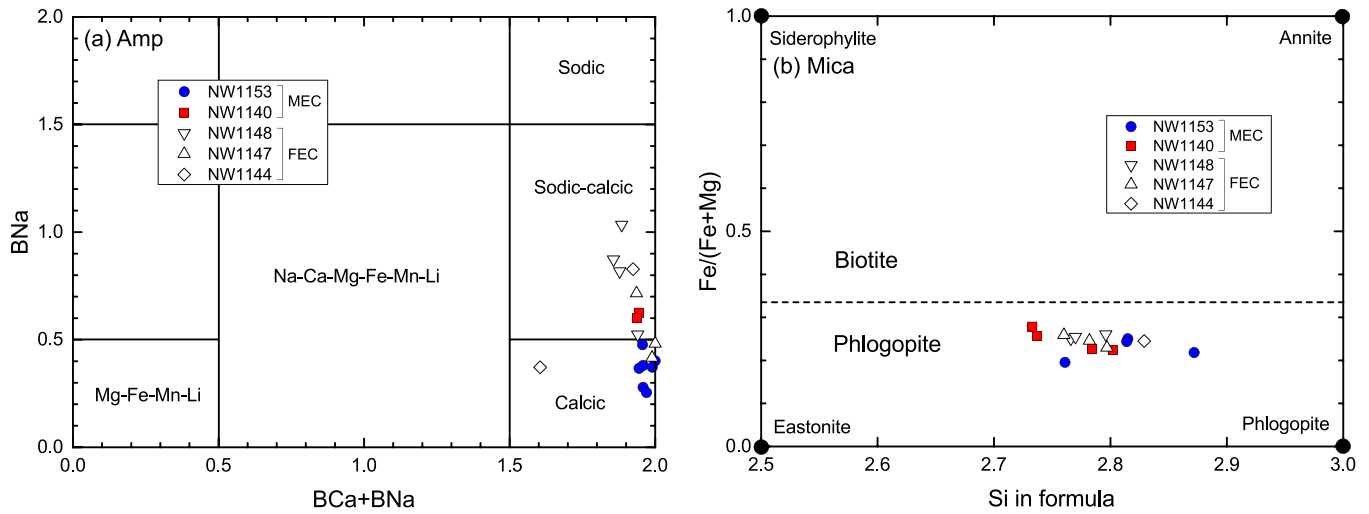
Figure 13. Compositions of amphibole (a) and mica (b). In the FEC the calcic Amp occurs at the retrograde symplectite, while the other sodic-calcic Amp occurs in the matrix.

stage should be even lower for the MEC, because most of its Amp (and possibly part of Phl) was formed during retrograde metamorphism (see captions in Figure 15).

In this context, these facts point to the potential role of water as a medium linking deformation to HP-UHP metamorphism. The most straightforward interpretation is that water was acquired externally with the aid of intense deformation and promoted the transition from HP MEC to UHP FEC during prograde and/or the early retrograde stages. Conversely, the lack of water infiltrating MEC may have hindered its transformation
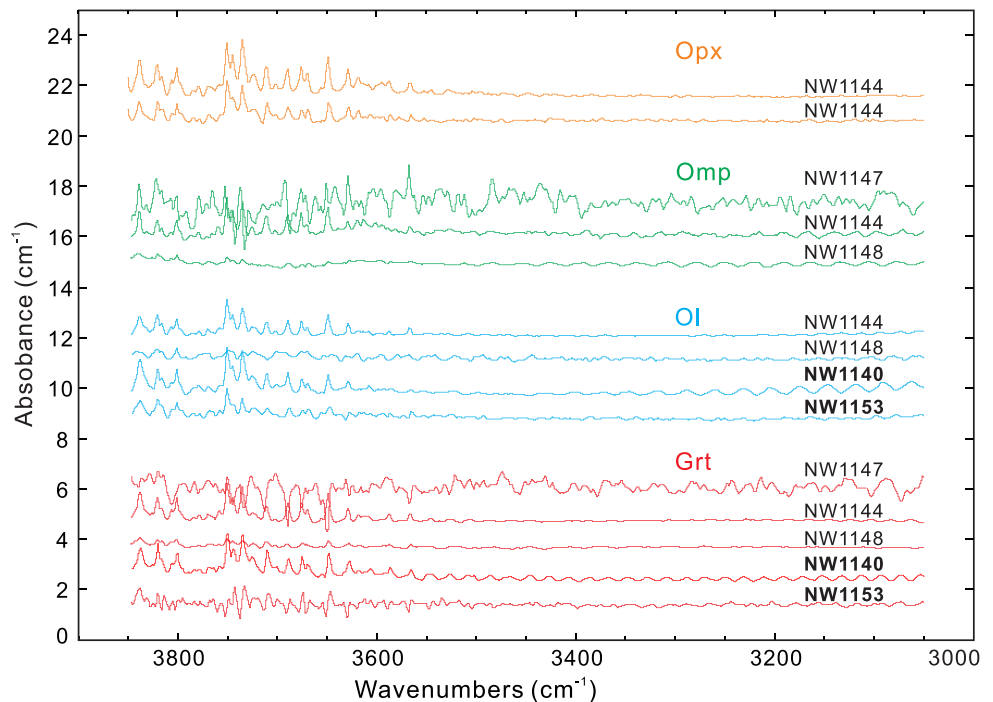
Figure 14. Representative IR spectra of single crystalline NAMs. The absorbance was normalized to 1 cm by the thickness of sample slice. The sample names in bold and plain fonts are MEC and FEC, respectively. The largest noise was observed in Sample NW1147 due to the sample having the smallest grain size and aperture used for IR analysis. The IR spectra of Omp and Opx in the MEC were not measured due to their small grain sizes in the coronitic rims around Ol.
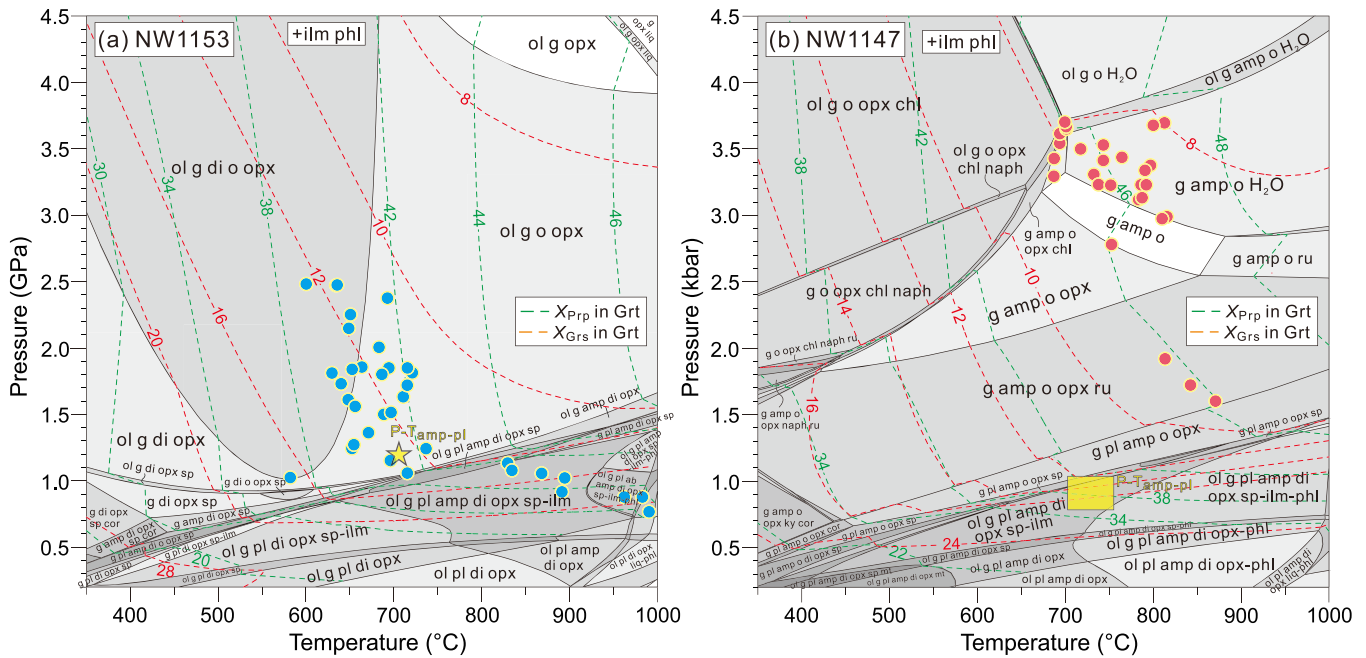
Figure 15. P-T pseudosections of (a) MEC Sample NW1153 and (b) FEC Sample NW1147. The green and red dashed lines are isopleths (colored labels) of Prp and Grs modal proportions in Grt, respectively. The cyan circles are the plots of Grt compositions in the mantle-to-rim regions to indicate the peak metamorphic conditions in the MEC. The higher Grs content in the Grt core and positive correlation between the Prp and Alm contents (Figures 12a, 12c, and 12d) suggest that the Grt core compositions in the MEC might have been mainly affected by the inverse accessibilities of Ca (sourced from Pl) and Mg-Fe (sourced from Ol) during the formation of Grt from Pl and Ol (see also Mørk (1986)). Therefore, the core compositions of Grt (not plotted) likely reflect the influence of the compositions of local domains and fail to determine the peak metamorphic conditions for the MEC. Instead, the narrow variations of the Grt compositions and occurrences of Omp inclusions in the mantle and rim, as well as the direct contact with Omp along the Grt rim (Figures 3c, 4a, 4b, and 12a), imply that the Grt mantle and rim regions are in textural equilibrium with neighboring minerals and can be used to estimate peak metamorphic P-T conditions for the MEC. On the contrary, the negative correlation between the narrowly ranged Alm and Prp contents in FEC (Figures 12b and 12d) implies that the whole Grt grain tends to attain an equilibrated state via Fe-Mg exchange with nearby minerals in the FEC. The core-to-rim Grt compositions are thus used to estimate the peak metamorphic conditions in the FEC (plots of red circles). The yellow star in (a) and rectangle in (b) denote the P-T conditions estimated from Amp-Pl thermobarometers. The estimation of effective bulk-rock compositions excludes the contribution of olivine which has a magmatic origin and exists as the reaction residue after eclogite-facies metamorphism. Furthermore, in the MEC, Amp almost only occurs in the Amp-Pl (or Phl) symplectite/corona (Figures 3c and 3d); its compositions are calcic (pargasite) suggesting it to be low-pressure amp (Figures 13a and S11a); and it grew mostly during the retrograde stage by hydration and topotactic replacement of Omp (Figures 9a and 9b). These facts thus point out that, to model the peak-stage metamorphism in the MEC, the amount of H_2O contained by retrograded Amp (and possibly parts of Phl) needs to be subtracted. In contrast, in the FEC, Amp occurs mostly in the matrix (Figures 5c and 5d); it has calcic-sodic compositions suggestive of high-pressure origin (Figures 13a and S11b); and shows no topotactic relationship with Omp (Figure S13). These results indicate that most Amp formed at peak and/or early-retrograde conditions and its H_2O needs to be included to model the peak-stage metamorphism in the FEC. The final effective bulk-rock compositions (mol.%) used for phase equilibria modeling are (a) NW1153: SiO_2 (46.90), TiO_2 (1.07), Al_2O_3 (9.30), FeO (12.64), O (0.21), MnO (0.20), MgO (17.79), CaO (9.12), Na_2O (2.08), K_2O (0.34) and H_2O (0.36); and (b) NW1147: SiO_2 (47.57), TiO_2 (0.68), Al_2O_3 (8.90), FeO (11.78), O (0.70), MnO (0.13), MgO (17.39), CaO (8.98), Na_2O (2.98), K_2O (0.11) and H_2O (0.77). The most remarkable differences between the two phase diagrams are that Amp is stable up to much higher pressures, chlorite (Chl) occurs at high-pressure and low-temperature condition, and free H_2O is present at high-pressure and high-temperature condition when bulk-rock water content is higher. Mineral abbreviations: garnet (g), omphacite (o), diopside (di), orthopyroxene (opx), olivine (ol), plagioclase (pl), amphibole (amp), chlorite (chl), phlogopite (phl), Na-phlogopite (naph), ilmenite (ilm), spinel (sp), rutile (ru), magnetite (mt), and potassium feldspar (ksp).

and preserved the metastable HP assemblage even at the P-T conditions suitable for UHP metamorphism (Jamtveit et al., 2016). In our eclogite outcrops, FEC occurs as mylonitic shear zones around MEC blocks (Figure 2) and eclogite bodies are surrounded by gabbro (Figure 1d). Therefore, we inferred two successive stages of fluid-induced eclogitization. First, gabbro transformed to MEC at HP condition during prograde path. The occurrence of Amp in the Grt core of MEC Sample NW1153 (Figure 3e) clearly implies that at least a minor amount of water is needed to hydrate gabbro. However, because both gabbro and MEC (e.g., NW1153) are weakly deformed (Mørk, 1985), the role of deformation in controlling the HP metamorphism of the gabbro protolith could be relatively weak and other factors may help to accomplish the gabbro to MEC transition (e.g., long duration). Second, MEC transforms to FEC transition at UHP condition

during prograde and/or early retrograde stages. The effect of water on enhancing the UHP metamorphism is manifested by the much higher water contents in the FEC compared to the MEC (see above).

The roles of deformation in promoting eclogite-facies metamorphism via the participation of water (i.e., triggering metamorphic reaction and enhancing its kinetics) and/or grain size reduction (i.e., increasing grain surface area and rock permeability) have also been reported for other granulite/gabbro-eclogite suites such as other localities in the WGR and Bergen Arcs, Norway (Austrheim, 1987, 2013; Austrheim et al., 1997; Austrheim & Griffin, 1985; Terry & Heidelbach, 2006), Zambezi Belt in Central Zambia (John & Schenk, 2003), and Marun-Keu Complex of the Polar Urals in Russia (Glodny et al., 2003), as well as granitic rocks at Yangkou in the Sulu UHP metamorphic belt (Fang & Yan, 2019). In these examples, HP-UHP eclogites often occur along ductile shear zones or as veins within granulite/gabbro, which are mainly interpreted as channelized fluid pathways within gabbro during HP-UHP metamorphism (Austrheim et al., 1997; John & Schenk, 2003). In a ductile regime, fluid can penetrate into the ductile shear zones from surrounding rocks more easily due to an increase of porosity (increasing permeability) where grain size is being reduced by intense ductile deformation (Wark & Watson, 2000) or through opening of microcavities (local dilatancies) caused by GBS during ductile deformation (i.e., creep cavitation) (Fusseis et al., 2009). The latter mechanism of water pumping has been evidenced in Ronda mylonitic peridotites and corroborated the fact that ductile flow can exerts a dynamic control on the long-term fluid (water) circulation in mantle shear zones (Precigout et al., 2017).

However, more recent studies have suggested that an efficient fluid infiltration often requires prior fractures or faults generated by deep earthquakes and the resulting fluid-driven HP-UHP metamorphism can produce weaker rocks, which subsequently deform viscously and form a ductile shear zone (Austrheim, 2013; Jamtveit et al., 2019; Petley-Ragan et al., 2018; Putnis et al., 2017). Such brittle deformation at the lower continental crust and subduction interface can be triggered as aftershocks by stress pulses and dynamically elevated strain rate generated by earthquakes in the shallow brittle regime (Cheng & Ben-Zion, 2019; Jamtveit et al., 2018; Petley-Ragan et al., 2019) and/or transiently but periodically increased pore fluid pressure related to the dehydration of adjacent portions of the downgoing plate (Broadwell et al., 2019; Viete et al., 2018). In our eclogites, the evidence for earthquake at HP condition is very likely reflected in the MEC where fragmented and internally strained Ol crystals with fractures infilled with small strain-free Opx grains (Figure 3f). This microstructure indicates that brittle deformation occurred precedingly and promoted the ensuing gabbro to MEC metamorphic reaction (consuming Ol to produce Opx) along the fractures probably caused by seismic loading (Austrheim et al., 2017). However, the occurrence of water infiltration along the fractures is not clear because of the absence of hydrous minerals in the fractures. Since more convincing evidence for seismic failures, such as pseudotachylyte, has not been found in the outcrops, the mechanism of earthquake induced eclogitization (especially MEC to FEC transition) remains speculative for our samples currently (Jamtveit et al., 2018).

Alternatively, long-term high differential stress (σ_{diff} or tectonic overpressure) may also be capable of generating the discrepant peak P-T conditions of MEC and FEC (Luisier et al., 2019; Mancktelow, 2008; Pleuger & Podladchikov, 2014; Reuber et al., 2016; Richter et al., 2016; Schmalholz & Podladchikov, 2014; Vrijmoed & Podladchikov, 2015; Wheeler, 2014). Based on this interpretation, UHP FEC is thought to be produced from HP MEC as the result of high σ_{diff} at HP conditions, while MEC is not affected by such high σ_{diff} due to stress partitioning and preserves its HP assemblage. The average peak-pressure gap between MEC and FEC is ~2 GPa, which falls into a reasonable range of tectonic overpressure in the continental collision zones (Reuber et al., 2016; Yamato & Brun, 2017).

However, the feasibilities of this interpretation in our eclogites are limited by two reasons. First, whether such high σ_{diff} can be effectively partitioned between MEC and FEC in a block as small as our eclogite outcrop and its effects on the extent of heterogeneous pressure distribution are still not clear. Based on a recent work by Luisier et al. (2019), a dramatic spatial variation of pressure over meters scale appears possible, in which the strong host rock mostly records pressure equal to the mean stress (σ_m, i.e., mean of maximum (σ_1) and minimum (σ_3) principal stresses) while the weak inclusion rock can preserve pressure close to σ_1 (see also Richter et al., 2016) when the inclusion's long axis is aligned at high angles (70–90°) to the σ_1 direction. Applying the average pressures of MEC (1.8 GPa, analog to strong host) and FEC (3.2 GPa, analog to weak inclusion), we obtained σ_1, σ_3, σ_{diff} ($\sigma_1 - \sigma_3$), and σ_m of 3.2, 0.4, 2.8 and 1.8 GPa, respectively.
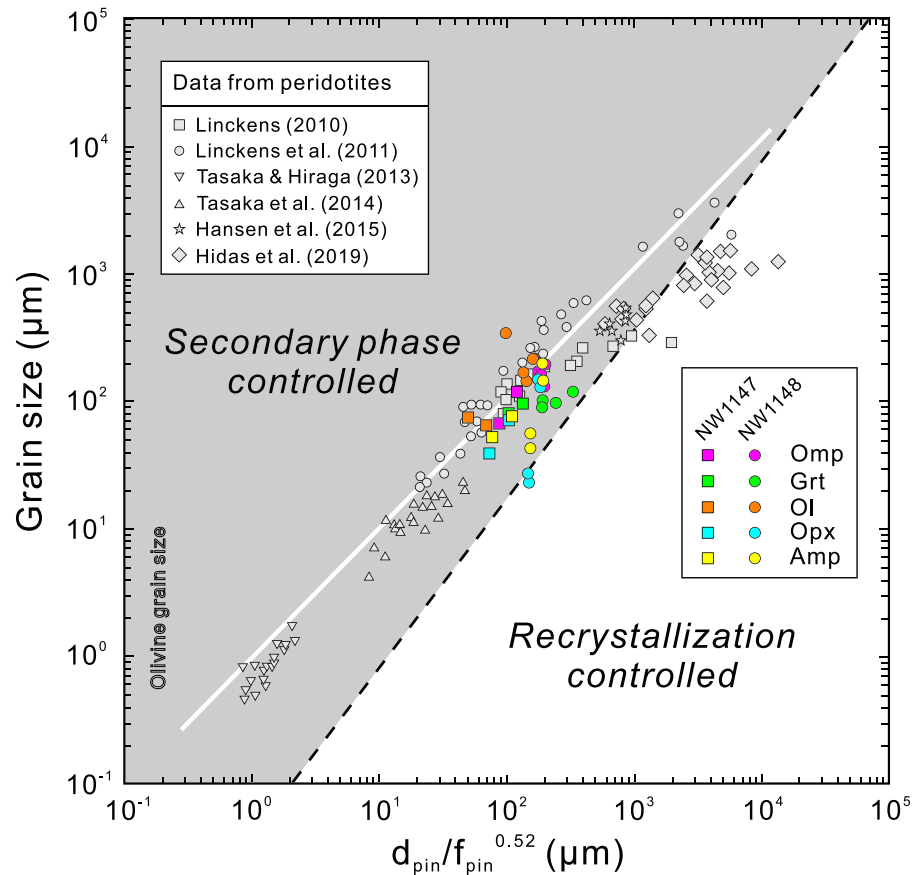
Figure 16. Zener diagram showing the area-weighted grain sizes of major phases (*y* axis) as a function of area-weighted grain size from all other phases and volume fraction of all other phases (*x* axis). Black dashed line is the boundary between secondary phase and dynamic recrystallization controlled grain size microstructures. While solid line is the fit line using a Zener parameter of 0.52 adopted from Tasaka et al. (2014). The background of the figure is modified after Hidas et al. (2019).

The estimated σ_{diff} (2.8 GPa) is much larger than σ_m (1.8 GPa) or confining pressure, suggesting that both MEC and FEC should be intensively fractured ("Goetze criterion," see Kohlstedt et al. (1995)), which is contradictory to the ductile deformation structures in the FEC. Besides, such high σ_{diff} (2.8 GPa) is neither plausible to occur in the lithospheric shear zones (σ_{diff} mostly <250 MPa, see Bürgmann & Dresen, 2008).

Second, a comparison between the σ_{diff} preserved in FEC and the peak-pressure gap between MEC and FEC can help assess the effect of σ_{diff}. If the σ_{diff} preserved in FEC is significantly smaller than one tenth of the peak-pressure gap (~200 MPa, calculated using a multiplying factor between tectonic overpressure and σ_{diff} provided by Wheeler (2014)), the FEC is more likely formed due to high lithostatic pressure rather than tectonic overpressure. The problem is that the exact value of σ_{diff} in the FEC is difficult to constrain because of the lack of effective piezometers for eclogite. However, based on a recrystallized grain size piezometer for dry olivine (Van der Wal et al., 1993)—which is applicable because of nearly absence of IR absorption peaks suggesting little water in Ol (Figure 14)—we estimated a σ_{diff} in the range of ~20–40 MPa from the 3-D olivine grain size (~100–330 μm, 2-D grain size (Figure 6) multiplied by a factor of 1.5 to correct the sectioning effect) for the ductile deformation of FEC. This stress range is an upper bound and real σ_{diff} should be much lower, because the FEC is a multiphase aggregate and the grain size of olivine is jointly reduced by the pinning of second phases besides stress (Figure 16). Therefore, although the smaller grain sizes in the FEC indeed indicate its higher σ_{diff} than that of the MEC, the loosely constrained σ_{diff} (<20–40 MPa) is still much lower than the required σ_{diff} (~200 MPa) to impose a considerable impact to the tectonic overpressure. This

relatively low stress value also concurs with the inference of nondislocation-based creep as the dominant deformation mechanism (see section below), because dislocation creep otherwise tends to dominate over diffusion creep at the high σ_{diff} (~200 MPa) and relevant grain size (~50–230 μm, Figure 6) (Frost & Ashby, 1982). Despite relatively small overpressure effect, this low σ_{diff} can still greatly promote the (U)HP metamorphism by enhancing the solid-state reaction (diffusion) kinetics (Keller et al., 2010) and the rate of pervasive fracturing and fluid infiltration process (Jamtveit et al., 2000; Jamtveit et al., 2016).

Transiently and repetitively high σ_{diff} episodes can actually exist if earthquake induced fractures are the precursors of subsequent ductile shear zones of FEC (Cheng & Ben-Zion, 2019; Jamtveit et al., 2018; Petley-Ragan et al., 2019). Transiently high σ_{diff} (and its induced transient overpressure) per se has been suggested to be able to produce grain-scale garnet overgrowth zones of increased pressure signature in the timescales of hundreds of years (Chu et al., 2017), however, its ability to form large-sized eclogite body (like our outcrops) is unlikely due to the short timescales of seismicity. Transiently high σ_{diff} associated with seismic activities plays a more impactful role—via introduction of fluids along the high stress induced fractures—only when the P-T conditions are appropriate for long-term eclogitization metamorphism (Austrheim, 2013; Engi et al., 2018; Jamtveit et al., 2016; Jamtveit et al., 2019; Putnis et al., 2017).

6.2. Deformation Mechanisms of Minerals

6.2.1. MEC

Because MEC is massive in structure, suggesting it is weakly deformed, its deformation mechanisms are only addressed briefly. First, evidence for coexisting brittle (fracturing mechanism, reflected by the fractured Ol and filling with small Opx grains) and ductile deformation (dislocation creep, indicated by the undulose extinctions) is found locally in the MEC (Figure 3f), implying that although the macrostructures were weakly modified by deformation (i.e. poorly developed foliation and lineation), a small amount of strain was still accommodated by some crystals in the MEC, probably via seismic loading (Austrheim et al., 2017). Thus, the weak but obvious CPOs of all major constituent minerals (Grt, Omp, Ol, Opx, and Amp) in the MEC (Figures 8a, 8b, 9a, and 9b) are not the consequences of deformation coeval with eclogitization. The inherence of preexisting CPOs (B-type like) in Ol can be inferred from the weak SPOs of euhedral Ol grains (Figure 3a) and their weak B-type like CPOs (Figures 8a and 8b), which were most likely formed by compaction or shearing during the crystallization and accumulation of Ol from magma (Cao et al., 2017; Yao et al., 2019). The good correlations of CPOs between Omp and Amp (Figures 9a and 9b) are strong evidence suggesting that the CPOs of Amp mainly resulted from topotactic replacement of Omp grains (Figure 3d) during retrograde metamorphism (Giuntoli et al., 2018). The formation mechanisms of the CPOs of Grt, Omp, and Opx are complicated and likely owing to the anisotropic growth of minerals under a macroscopic deviatoric stress field (preliminary results of our following study).

6.2.2. FEC

The deformation mechanisms and geneses of CPOs in the major constituent minerals in the FEC are important because FEC accommodates most strain during the ductile deformation coincident with and/or postdating eclogitization metamorphism. Based on the microstructural analysis, we proposed that nondislocation-based creep mechanisms—such as diffusion creep, grain and phase boundary sliding, and rigid-body-like rotation—are the dominant contributors to accommodate plastic strain and develop mineral CPOs in the FEC. The evidence for this deduction is listed below.

First, intragranular misorientation angles (dominantly <1°, Figures 11 and S3–S5) and GOS values (<1°, Figures 6c and 6d) are very low in the grains of all major phases (Grt, Omp, Ol, Opx, and Amp). These results indicate that dislocation creep—the main contributor to the geometrically distorted crystal lattice (Passchier & Trouw, 2005)—is not prevalently activated during ductile deformation. Evidence for dislocation creep is mostly found in a few large Ol, Opx, and Amp grains that display relatively large intragranular misorientation angles (2–10°, Figures S3–S5) and greater GOS (>1°, Figures 6c and 6d), suggesting that dislocation creep is locally prevalent in the domains where higher stress is concentrated and strain is generally not accommodated by other mechanisms (Frost & Ashby, 1982). The weak but discernable positive correlations between GOS and grain size for individual phases (Figure 6d) illustrate that dislocation creep is generally more prominent at larger grains. Besides, the larger GOS values found in Opx and Amp, which have also greater shape factors compared to Ol, Omp and Grt (Figure 6c, overall Opx > Amp > Ol > Omp > Grt), indicate that dislocation creep can induce more sinuous grain boundaries via piling up of dislocations or grain

boundary migration (Passchier & Trouw, 2005). Alternatively, the sinuous grain or phase boundaries—which can also be formed by mineral dissolution and precipitation accompanied with metamorphic reactions, especially for Opx and Amp—may cause stress to concentrate at their irregularities (e.g., ledges or steps) and thus enhance the activity of dislocations. Compared to Subtype-I FEC, the low GOS values of Grt, Omp, and Ol in the Subtype-II FEC (Figures 6c and 6d) also agree with their smaller grain sizes (Figures 6b and 6d) and suggest even weaker dislocation activities.

Therefore, dislocation creep is not considered as the major contributor to the mineral CPOs in the FEC. The weak CPO strengths of Omp, Ol, Opx, and Amp in most FEC samples (J-index <2.1, M-index <0.06; Figures 8 and 9 and S2) also disfavor dislocation creep as a dominant deformation mechanism which actually results in a much stronger CPO if one dominant slip system was activated (Karato, S.-i., 2008). The exception is the CPOs of Grt, which are always very weak even via dislocation creep owing to their 66 slip systems and cubic symmetry (Ando et al., 1993; Ji et al., 2003; Mainprice et al., 2004). Besides, the lack of the dependence of CPO strength (M-index and J-index) on grain size (Figure 10) also hints that the CPOs should mainly not result from dislocation creep which is able to elevate the CPO strength with increasing grain size. The distribution patterns of the intragranular misorientation axes in the crystal coordinates reveal mainly [100](001) and [001](100) slip systems in the Ol (Figures S6a–S8a), mostly [010](100), [001](100), [001](010) and [001]{210} slip systems in the Opx (Figures S6b–S8b), mainly [001](100), [001](010), [001]{hk0} and [100](010) slip systems in Omp (Figures S6d–S8d), and mostly [001](010), [001](100) and [100](010) slip systems in the Amp (Figures S6e–S8e). The coexistence of these multiple slip systems in a mineral can contribute to weak CPO strengths of Ol, Omp, Opx, and Amp. However, an overall poor consistency of the CPOs between the grains with 2–10° misorientations and the complete grain sets (Figures S6–S8) may argue against a significant contribution of dislocation creep to the bulk-rock CPOs. Exceptions are the domains containing many Ol, Amp, and Opx grains with 2–10° misorientations, which display the CPOs somewhat similar to those of the complete grain sets (Figures S7b, S7e, S8a, and S8e), implying that the role of dislocation creep on the CPO development can be locally important, especially for Ol, Amp, and Opx. Nevertheless, it should be admitted that such comparison of CPOs may have an inaccuracy, because the numbers of grains with misorientation angles of 2–10° are small ($N < 150$) and their CPOs may not be representative enough.

Second, shape factors (~1.2–1.7, Figures 6a and 6c) and aspect ratios (~1.4–2.3, Figures 6a and 6b) are very small and four grain or phase junctions are prevalent in almost all major phases (Grt, Omp, Ol, Opx, and Amp) (Figures 4c–4e). The small shape factors and aspect ratios indicate that the grain boundaries and shapes are dominantly straight and equigranular, respectively. These grain characteristics can greatly ease and facilitate the sliding of crystals along their common grain or phase boundaries, as supported by the frequent occurrences of four (even five) grain junctions which commonly represent a transient stage of GBS process during large strain deformation (Ashby & Verrall, 1973). Owing to the lack of intragranular misorientations of 2–10° in the grains that forms the four (or five) grain or phase junctions (cf. Figures 4c, 4d, and 10), the GBS process is likely assisted mainly by diffusion creep and categorized as Lifshitz GBS (Langdon, 2006).

In a multiphase assemblage such as peridotite, GBS process can effectively promote phase mixing (Cross & Skemer, 2017; Linckens et al., 2014) and inhibit grain growth through boundary migration by pinning the grain or phase boundaries of each phases (Linckens et al., 2011; Linckens et al., 2015). The sufficiently small grain sizes resulted from phase mixing and pinning can tremendously reduce the viscosity and accelerate the strain localization by promoting the grain-size-sensitive diffusion creep (Maruyama & Hiraga, 2017b; Tasaka et al., 2014; Warren & Hirth, 2006). As an analogy, the multiphase FEC presents grain sizes (Omp, Grt, Ol, Opx, and Amp) that are controlled mainly by the second phases (all other phases) in the similar manner as the peridotites from natural mantle shear zones and the analogs from deformation experiments (Figure 16). This result agrees with the findings from peridotites and thus supports the prevalence of GBS and resulting phase mixing process in the FEC. Because ductile deformation is considered to be concurrent with and to promote the eclogite-facies metamorphism (see section 6.1), the accompanied metamorphic reactions (forming fine-grained new phases) are also expected to enhance the phase mixing process in the FEC (Delle Piane et al., 2007; Mansard et al., 2020; Newman et al., 1999; Prigent et al., 2018). Recently, based on the deformation experiments using Ol-Cpx aggregates, Zhao et al. (2019) proposed that, independent of small grain pinning effect, phase boundaries sliding (PBS) per se can also substantially enhance the rate of deformation due

to the low viscosity, fast diffusivity and reaction rate along the phase boundaries. Given the great efficiency of PBS and the abundance of phase boundaries between multiple phases in the FEC, it is reasonable to consider that PBS is an important and even dominant mechanism responsible for the deformation of FEC.

The shape factor and aspect ratio are positively correlated and their values differ among phases, overall Grt < Omp < Ol < Amp < Opx (Figure 6a), hinting that the importance of GBS and PBS in various phases may decrease in a similar order which is opposite to the roles of dislocation creep (see above). Compared to Subtype-I FEC, the smaller grain size, shape factor and aspect ratio of Grt, Omp and Ol (Figure 6) and better phase mixing (Figures 4c and 4d) in the Subtype-II FEC signify more prominent roles of GBS and PBS in this FEC subtype.

Recent studies on experimental deformation of peridotite and its analogs suggested that GBS and PBS accompanied with diffusion creep are also capable of producing weak but distinct CPOs of Ol (Maruyama & Hiraga, 2017b; Miyazaki et al., 2013; Sundberg & Cooper, 2008; Zhao et al., 2019). Because the low-index plane boundaries tend to have lower viscosity than other general grain boundaries, preferential sliding along these grain and phase boundaries would result in the development of a CPO with low-index planes and axes aligning subparallel to the structural reference frame (i.e., X, Y, and Z axes) but the CPO strength is weak owing to the concomitant diffusion creep (Maruyama & Hiraga, 2017b). In the FEC, CPOs of Ol, Opx, Omp and Amp are found in most samples (Figures 8c–8g and 9c–9g). These CPOs are mostly weak with structural reference frame following the typical low-index planes and axes of Ol, Opx, Omp, and Amp—especially for Omp and Amp, their CPO patterns are typical and also commonly found in the eclogites, blueschists, and amphibolites from other HP-UHP localities (e.g., Abalos, 1997; Bascou et al., 2001; Cao et al., 2011; Cao et al., 2013, 2014; Cao & Jung, 2016; Godard & van Roermund, 1995; Ha et al., 2018; Ji et al., 2013; Keppler, 2018; Keppler et al., 2015; Keppler et al., 2016; Keppler et al., 2017; Kitamura, 2006; Kurz et al., 2004; Neufeld et al., 2008; Tatham et al., 2008)—indicating that these CPOs are likely the products of GBS and PBS processes. It is noted that this argument is not applicable to Grt in the FEC, because the weak CPOs of Grt display no obvious correlations between the low-index planes or axes and the structural reference frame (Figures 8c–8g). The absence of the correlations of CPOs between Omp and Amp (Figures 9c–9g) as well as between neighboring Omp and Amp grains akin to those of MEC (Figure S13) also disapproves the topotactic replacement as the CPO formation mechanism of Amp in the FEC.

Third, pronounced SPOs are developed in Grt, Amp, Omp, and Ol (Figures 7a, 7c, 7e, and S1) and the long axes of their grains tend to align subparallel to the foliation with increasing aspect ratios (Figures 7b, 7d, and 7f). These results indicate that the shape-anisotropic grains (Grt, Amp, Omp, and Ol)—which could be formed mainly by diffusion and less by dislocation creep (as discussed above)—are rotated to align their long axes subparallel to the shear plane (Cao et al., 2014; Gay, 1968; Masuda et al., 1995; Passchier, 1987). The larger aspect ratios the grains have, the more readily they are rotated and form a stronger SPO (Ildefonse et al., 1990). There is a lack of dependence of aspect ratio on grain size (Figure 6b) suggesting that the easiness of grain rotation may be mainly controlled by aspect ratio. The grain rotation might have also likely occurred for Opx during deformation, although its SPOs are not clear due to limited number of grains (Figure S1). Recent deformation experiments on Ol-Cpx aggregates suggested that rigid-body-like rotation is actually a concomitant and complementary process with the GBS and PBS, which both preferentially occur along the low-index plane boundaries and are required to develop both SPO and CPO during diffusion creep (Maruyama & Hiraga, 2017a, 2017b). Based on the previous experimental work and the observations in this study, we consider that the FEC and its CPOs of major phases (Grt, Omp, Ol, Opx, and Amp) were mainly formed by the same deformation mechanisms above.

6.3. Implications for Tectonic Setting and Numerical Modeling

Based on this study, the mixture of different peak metamorphic facies as represented by the coexistence of metastable HP MEC (or gabbro) and UHP FEC can be attributed to the heterogeneous extent of deformation and availability of fluid, instead of the tectonic juxtaposition. This inference thus implies that the gabbro-to-eclogite and MEC-to-FEC transformations may occur around the Moho beneath a thickened orogenic belt in response to continental collision (see review of Austrheim (2013)), and may not require the setting as continental subduction interface which has been commonly proposed to interpret the mixing formation of tectonic mélange by channel flow (see Introduction section). This speculation tends to be

reasonable but needs more compelling evidence, especially by comparing the metamorphic P-T conditions and histories of the eclogites and their surrounding migmatitic gneisses and by considering the possibility whether such deformation and fluid controlled metastability can also be realized at the continental subduction channel.

Recently, Palin et al. (2017) proposed that the metastable preservation of low pressure assemblage may be widespread for the felsic component of the crust during subduction and/or burial. Here, we extended the conclusion by Palin et al. (2017) to that not only felsic component but also mafic to ultramafic components (e.g., gabbro and eclogite) can be metastable continuously throughout the tectonic cycles of subduction and collision zones. The effects of deformation and associated mobilizing fluid on controlling reaction kinetics (e.g., catalyzing eclogitization) and variable transformation of rocks at depth (e.g., gabbro-to-eclogite transition) need be considered in the geodynamic and petrological modeling studies, which are currently inadequate under the conventional assumption of equilibrium metamorphism. Besides, the deformation mechanisms inferred from FEC indicate that the subducting crust (or continental Moho) can be deformed to a large extent in regimes requiring diffusion creep, GBS/PBS and rigid-body-like rotation (Wassmann & Stockhert, 2013), which can considerably affect the interplate coupling and channel flow along the subduction interface or the rheological strength of continental Moho beneath the collision zone (Agard et al., 2016). Unfortunately, these nondislocation-based deformation mechanisms are commonly not included in the current geodynamic modelings, which conventionally use non-Newtonian rheology (e.g., power law behavior for dislocation creep). This fact undermines the capabilities of current models to study the viscoplastic flow of various components of the subduction and collision zones. Therefore, the flow laws of diffusion creep, GBS/PBS, and rigid-body-like rotation of the crustal rocks at the relevant physicochemical conditions need to be constrained by innovative experiments before incorporated in future geodynamic simulations.

7. Conclusions

The eclogite in the Flem Gabbro from Flemsøya Island of the WGR in Norway is a rare olivine-bearing eclogite derived from olivine gabbro cumulate. The eclogite can be divided into two distinct categories: weakly deformed MEC and strongly deformed FEC. The MEC preserved prograde metamorphism to the peak stage at ~600–750 °C and ~1.0–2.5 GPa, whereas FEC reflects a retrograde metamorphic path from ~700–820 °C and ~2.7–3.7 GPa (peak stage) to ~710–760 °C and ~0.8–1.0 GPa (late postpeak stage). The different peak P-T conditions of MEC (HP condition) and FEC (UHP condition) likely reflect (1) deformation-enhanced eclogitization metamorphism (HP to UHP transition) via the addition of external water during subduction/burial and/or early exhumation stages and (2) metastable preservation of lower-pressure assemblages (e.g., MEC and/or gabbro) due to the local lack of deformation and fluid access at the deep subduction interface or at the continental Moho beneath collision zones (UHP conditions).

The MEC is weakly deformed due to small strain, implying that their weak mineral CPOs are likely related to the preexisting CPO (Ol), anisotropic growth of minerals under a macroscopic deviatoric stress field (Grt, Omp, and Opx) and CPO inheritance by topotaxial replacement (Amp). In contrast, the deformation microstructures in the FEC—small intragranular misorientation angles, shape factors and aspect ratios, weak CPOs (N.B. this argument is not applicable to Grt), the prevalence of four (even five) grain junctions, and the pattern that the long axes of grains with elongated or flatten grains tend to align at lower angles to foliation for the major constituent phases (Grt, Omp, Ol, Opx, and Amp)—suggest that nondislocation-based creep mechanisms, such as diffusion creep, grain and phase boundary sliding, and rigid-body-like rotation, play dominant roles in accommodating large viscous strains, developing mineral CPOs and governing the rheological properties of eclogite. Notably, a few Ol, Opx, and Amp grains preserving large intragranular misorientation angles indicate that dislocation creep can be locally prominent under a nondislocation-based deformation dominated regime.

The metamorphic metastability and nondislocation-based deformation mechanisms can considerably affect the interplate coupling and channel flow along a subduction interface or the rheological strength of continental Moho beneath the collision zone. Therefore, more sophisticated numerical models combining metastability-based (i.e., preservation of lower-pressure assemblage at HP-UHP conditions) and nondislocation-based creep mechanisms of the subducting crust as the dominant deformation mechanisms are needed for future investigations of the petrology and geodynamics of the subduction and collision zones.

References

Abalos, B. (1997). Omphacite fabric variation in the Cabo Ortegal eclogite (NW Spain): Relationships with strain symmetry during high-pressure deformation. *Journal of Structural Geology*, *19*(5), 621–637. https://doi.org/10.1016/S0191-8141(97)00001-1

Agard, P., Yamato, P., Soret, M., Prigent, C., Guillot, S., Plunder, A., et al. (2016). Plate interface rheological switches during subduction infancy: Control on slab penetration and metamorphic sole formation. *Earth and Planetary Science Letters*, *451*, 208–220. https://doi.org/10.1016/j.epsl.2016.06.054

Andersen, T. B. (1998). Extensional tectonics in the caledonides of southern Norway, an overview. *Tectonophysics*, *285*(3–4), 333–351. https://doi.org/10.1016/S0040-1951(97)00277-1

Andersen, T. B., & Austrheim, H. (2006). Fossil earthquakes recorded by pseudotachylytes in mantle peridotite from the Alpine subduction complex of Corsica. *Earth and Planetary Science Letters*, *242*(1–2), 58–72. https://doi.org/10.1016/j.epsl.2005.11.058

Andersen, T. B., Jamtveit, B., Dewey, J. F., & Swensson, E. (1991). Subduction and eduction of continental crust: Major mechanisms during continent-continent collision and orogenic extensional collapse, a model based on the south Norwegian Caledonides. *Terra Nova*, *3*(3), 303–310. https://doi.org/10.1111/j.1365-3121.1991.tb00148.x

Ando, J., Fujino, K., & Takeshita, T. (1993). Dislocation microstructures in naturally deformed silicate garnets. *Physics of the Earth and Planetary Interiors*, *80*(3–4), 105–116.

Angiboust, S., Agard, P., Raimbourg, H., Yamato, P., & Huet, B. (2011). Subduction interface processes recorded by eclogite-facies shear zones. *(Monviso, W. Alps), Lithos*, *127*(1–2), 222–238. https://doi.org/10.1016/j.lithos.2011.09.004

Angiboust, S., Kirsch, J., Oncken, O., Glodny, J., Monié, P., & Rybacki, E. (2015). Probing the transition between seismically coupled and decoupled segments along an ancient subduction interface. *Geochemistry, Geophysics, Geosystems*, *16*(6), 1905–1922. https://doi.org/10.1002/2015GC005776

Ashby, M. F., & Verrall, R. A. (1973). Diffusion-accommodated flow and superplasticity. *Acta Metallurgica*, *21*(2), 149–163. https://doi.org/10.1016/0001-6160(73)90057-6

Audet, P., & Kim, Y. (2016). Teleseismic constraints on the geological environment of deep episodic slow earthquakes in subduction zone forearcs: A review. *Tectonophysics*, *670*, 1–15. https://doi.org/10.1016/j.tecto.2016.01.005

Austrheim, H. (1987). Eclogitization of lower crustal granulites by fluid migration through shear zones. *Earth and Planetary Science Letters*, *81*(2–3), 221–232. https://doi.org/10.1016/0012-821x(87)90158-0

Austrheim, H. (2013). Fluid and deformation induced metamorphic processes around Moho beneath continent collision zones: Examples from the exposed root zone of the Caledonian mountain belt. *W-Norway, Tectonophysics*, *609*, 620–635. https://doi.org/10.1016/j.tecto.2013.08.030

Austrheim, H., & Boundy, T. M. (1994). Pseudotachylytes generated during seismic faulting and eclogitization of the deep crust. *Science*, *265*(5168), 82–83. https://doi.org/10.1126/science.265.5168.82

Austrheim, H., Dunkel, K. G., Plümper, O., Ildefonse, B., Liu, Y., & Jamtveit, B. (2017). Fragmentation of wall rock garnets during deep crustal earthquakes. *Science Advances*, *3*(2), e1602067. https://doi.org/10.1126/sciadv.1602067

Austrheim, H., Erambert, M., & Engvik, A. K. (1997). Processing of crust in the root of the Caledonian continental collision zone: The role of eclogitization. *Tectonophysics*, *273*(1–2), 129–153. https://doi.org/10.1016/S0040-1951(96)00291-0

Austrheim, H., & Griffin, W. L. (1985). Shear deformation and eclogite formation within granulite-facies anorthosites of the Bergen arcs, western Norway. *Chemical Geology*, *50*(1), 267–281. https://doi.org/10.1016/0009-2541(85)90124-X

Bachmann, F., Hielscher, R., & Schaeben, H. (2010). Texture analysis with MTEX—Free and open source software toolbox. *Solid State Phenomena*, *160*, 63–68. https://doi.org/10.4028/www.scientific.net/SSP.160.63

Bachmann, R., Oncken, O., Glodny, J., Seifert, W., Georgieva, V., & Sudo, M. (2009). Exposed plate interface in the European Alps reveals fabric styles and gradients related to an ancient seismogenic coupling zone. *Journal of Geophysical Research: Solid Earth*, *114*(B5), 1–23. https://doi.org/10.1029/2008JB005927

Baldwin, S. L., Monteleone, B. D., Webb, L. E., Fitzgerald, P. G., Grove, M., & Hill, E. J. (2004). Pliocene eclogite exhumation at plate tectonic rates in eastern Papua New Guinea. *Nature*, *431*(7006), 263–267. https://doi.org/10.1038/nature02846

Bascou, J., Barruol, G., Vauchez, A., Mainprice, D., & Egydio-Silva, M. (2001). EBSD-measured lattice-preferred orientations and seismic properties of eclogites. *Tectonophysics*, *342*(1–2), 61–80. https://doi.org/10.1016/S0040-1951(01)00156-1

Boundy, T. M., Fountain, D. M., & Austrheim, H. (1992). Structural development and petrofabrics of eclogite facies shear zones, Bergen Arcs, western Norway: Implications for deep crustal deformational processes. *Journal of Metamorphic Geology*, *10*(2), 127–146. https://doi.org/10.1111/j.1525-1314.1992.tb00075.x

Broadwell, K. S., Locatelli, M., Verlaguet, A., Agard, P., & Caddick, M. J. (2019). Transient and periodic brittle deformation of eclogites during intermediate-depth subduction. *Earth and Planetary Science Letters*, *521*, 91–102. https://doi.org/10.1016/j.epsl.2019.06.008

Brodie, K. H., & Rutter, E. H. (1985). On the relationship between deformation and metamorphism, with special reference to the behavior of basic rocks. In A. B. Thompson, D. C. Rubie, & M. B. Bayly (Eds.), *Metamorphic reactions: kinetics, textures, and deformation. Advances in physical geochemistry, v. 4*, (pp. 138–179). New York: Springer-Verlag.

Bunge, H. (1982). *Texture analysis in materials science: Mathematical models*. London: Butterworths.

Bürgmann, R., & Dresen, G. (2008). Rheology of the lower crust and upper mantle: Evidence from rock mechanics, geodesy, and field observations. *Annual Review of Earth and Planetary Sciences*, *36*(1), 531–567. https://doi.org/10.1146/annurev.earth.36.031207.124326

Butler, J. P., Jamieson, R. A., Steenkamp, H. M., & Robinson, P. (2013). Discovery of coesite–eclogite from the Nordøyane UHP domain, Western Gneiss Region, Norway: Field relations, metamorphic history, and tectonic significance. *Journal of Metamorphic Geology*, *31*(2), 147–163. https://doi.org/10.1111/jmg.12004

Cao, Y., & Jung, H. (2016). Seismic properties of subducting oceanic crust: Constraints from natural lawsonite-bearing blueschist and eclogite in Sivrihisar Massif. *Turkey, Physics of the Earth and Planetary Interiors*, *250*, 12–30. https://doi.org/10.1016/j.pepi.2015.10.003

Cao, Y., Jung, H., & Song, S. (2017). Olivine fabrics and tectonic evolution of fore-arc mantles: A natural perspective from the Songshugou dunite and harzburgite in the Qinling orogenic belt, Central China. *Geochemistry, Geophysics, Geosystems*, *18*(3), 907–934. https://doi.org/10.1002/2016gc006614

Cao, Y., Jung, H., & Song, S. G. (2013). Petro-fabrics and seismic properties of blueschist and eclogite in the North Qilian suture zone, NW China: Implications for the low-velocity upper layer in subducting slab, trench-parallel seismic anisotropy, and eclogite detectability in the subduction zone. *Journal of Geophysical Research: Solid Earth*, *118*(6), 3037–3058. https://doi.org/10.1002/Jgrb.50212

Cao, Y., Jung, H., & Song, S. G. (2014), Microstructures and petro-fabrics of lawsonite blueschist in the North Qilian suture zone, NW China: Implications for seismic anisotropy of subducting oceanic crust, *Tectonophysics*, *628*(0), 140–157, doi:https://doi.org/10.1016/j.tecto.2014.04.028.

Cao, Y., Song, S. G., Niu, Y. L., Jung, H., & Jin, Z. M. (2011). Variation of mineral composition, fabric and oxygen fugacity from massive to foliated eclogites during exhumation of subducted ocean crust in the North Qilian suture zone, NW China. *Journal of Metamorphic Geology*, *29*(7), 699–720. https://doi.org/10.1111/j.1525-1314.2011.00937.x

Carswell, D. A., van Roermund, H. L. M., & de Vries, D. F. W. (2006). Scandian ultrahigh-pressure metamorphism of Proterozoic basement rocks on Fjørtoft and Otrøy, Western Gneiss Region, Norway. *International Geology Review*, *48*(11), 957–977. https://doi.org/10.2747/0020-6814.48.11.957

Cheng, Y., & Ben-Zion, Y. (2019). Transient brittle-ductile transition depth induced by moderate-large earthquakes in southern and Baja California. *Geophysical Research Letters*, *46*(20), 11,109–11,117. https://doi.org/10.1029/2019gl084315

Chu, X., Ague, J. J., Podladchikov, Y. Y., & Tian, M. (2017). Ultrafast eclogite formation via melting-induced overpressure. *Earth and Planetary Science Letters*, *479*(Supplement C, 1–17. https://doi.org/10.1016/j.epsl.2017.09.007

Cross, A. J., & Skemer, P. (2017). Ultramylonite generation via phase mixing in high-strain experiments. *Journal of Geophysical Research: Solid Earth*, *122*, 1744–1759. https://doi.org/10.1002/2016jb013801

Cuthbert, S. J., Carswell, D. A., Krogh-Ravna, E. J., & Wain, A. (2000). Eclogites and eclogites in the Western Gneiss Region, Norwegian Caledonides. *Lithos*, *52*(1–4), 165–195. https://doi.org/10.1016/S0024-4937(99)00090-0

Davis, P. B., & Whitney, D. L. (2006). Petrogenesis of lawsonite and epidote eclogite and blueschist, Sivrihisar Massif, Turkey. *Journal of Metamorphic Geology*, *24*(9), 823–849. https://doi.org/10.1111/j.1525-1314.2006.00671.x

de Capitani, C., & Petrakakis, K. (2010). The computation of equilibrium assemblage diagrams with Theriak/Domino software. *American Mineralogist*, *95*(7), 1006–1016. https://doi.org/10.2138/am.2010.3354

Delle Piane, C., Burlini, L., & Grobety, B. (2007). Reaction-induced strain localization: Torsion experiments on dolomite. *Earth and Planetary Science Letters*, *256*(1–2), 36–46. https://doi.org/10.1016/j.epsl.2007.01.012

Dobrzhinetskaya, L. F., Eide, E. A., Larsen, R. B., Sturt, B. A., Tronnes, R. G., Smith, D. C., et al. (1995). Microdiamond in high-grade metamorphic rocks of the Western gneiss region, Norway. *Geology*, *23*(7), 597–600. https://doi.org/10.1130/0091-7613(1995)023<0597:Mihgmr>2.3.Co;2

Du, J. X., Zhang, L. F., Bader, T., Chen, Z. Y., & Lü, Z. (2014). Metamorphic evolution of relict lawsonite-bearing eclogites from the (U) HP metamorphic belt in the Chinese southwestern Tianshan. *Journal of Metamorphic Geology*, *32*(6), 575–598. https://doi.org/10.1111/jmg.12080

Duarte, J. C., Schellart, W. P., & Cruden, A. R. (2015). How weak is the subduction zone interface? *Geophysical Research Letters*, *42*(8), 2664–2673. https://doi.org/10.1002/2014gl062876

Engi, M., Giuntoli, F., Lanari, P., Burn, M., Kunz, B., & Bouvier, A. S. (2018). Pervasive eclogitization due to brittle deformation and rehydration of subducted basement: Effects on continental recycling? *Geochemistry, Geophysics, Geosystems*, *19*(3), 865–881. https://doi.org/10.1002/2017GC007215

Engvik, A. K., Andersen, T. B., & Wachmann, M. (2007). Inhomogeneous deformation in deeply buried continental crust, an example from the eclogite-facies province of the Western Gneiss Region, Norway. *Norwegian Journal of Geology*, *87*(4), 373–389.

Ernst, W. G. (2016). Franciscan mélanges: Coherent blocks in a low-density, ductile matrix. *International Geology Review*, *58*(5), 626–642. https://doi.org/10.1080/00206814.2015.1108879

Fang, A., & Yan, Z. Z. (2019). Deformation-enhanced HP-UHP metamorphic transformation of two-pyroxene granite in ductile shear zones at Yangkou, Sulu UHP metamorphic belt, China. *Journal of Structural Geology*, *124*, 8–22. https://doi.org/10.1016/j.jsg.2019.04.003

Frost, H. J., & Ashby, M. F. (1982). *Deformation-mechanism maps: the plasticity and creep of metals and ceramics*. New York: Pergamon Press.

Fusseis, F., Regenauer-Lieb, K., Liu, J., Hough, R. M., & De Carlo, F. (2009). Creep cavitation can establish a dynamic granular fluid pump in ductile shear zones. *Nature*, *459*, 974. https://doi.org/10.1038/nature08051

Gay, N. C. (1968), Pure shear and simple shear deformation of inhomogeneous viscous fluids. 1. Theory, *Tectonophysics*, *5*(3), 211-&, https://doi.org/10.1016/0040-1951(68)90065-6.

Giuntoli, F., Menegon, L., Warren, C. J., & Brown, M. (2018). Replacement reactions and deformation by dissolution and precipitation processes in amphibolites. *Journal of Metamorphic Geology*, *36*(9), 1263–1286. https://doi.org/10.1111/jmg.12445

Glodny, J., Austrheim, H., Molina, J. F., Rusin, A. I., & Seward, D. (2003). Rb/Sr record of fluid-rock interaction in eclogites: The Marun-Keu complex, polar Urals, Russia. *Geochimica et Cosmochimica Acta*, *67*(22), 4353–4371.

Godard, G., & van Roermund, H. L. M. (1995). Deformation-induced clinopyroxene fabrics from eclogites. *Journal of Structural Geology*, *17*(10), 1425–1443. https://doi.org/10.1016/0191-8141(95)00038-F

Green, E. C. R., White, R. W., Diener, J. F. A., Powell, R., Holland, T. J. B., & Palin, R. M. (2016). Activity–composition relations for the calculation of partial melting equilibria in metabasic rocks. *Journal of Metamorphic Geology*, *34*(9), 845–869. https://doi.org/10.1111/jmg.12211

Ha, Y., Jung, H., & Raymond, L. A. (2018). Deformation fabrics of glaucophane schists and implications for seismic anisotropy: The importance of lattice preferred orientation of phengite. *International Geology Review*, *1-18*. https://doi.org/10.1080/00206814.2018.1449142

Hacker, B. (2007). Ascent of the ultrahigh-pressure Western Gneiss Region, Norway. *Geological Society of America Special Papers*, *419*, 171–184. https://doi.org/10.1130/2006.2419(09)

Hacker, B. R., Andersen, T. B., Johnston, S., Kylander-Clark, A. R. C., Peterman, E. M., Walsh, E. O., & Young, D. (2010). High-temperature deformation during continental-margin subduction & exhumation: The ultrahigh-pressure Western Gneiss Region of Norway. *Tectonophysics*, *480*(1–4), 149–171. https://doi.org/10.1016/j.tecto.2009.08.012

Hacker, B. R., & Gans, P. B. (2005). Continental collisions and the creation of ultrahigh-pressure terranes: Petrology and thermochronology of nappes in the central Scandinavian Caledonides. *Geological Society of America Bulletin*, *117*(1–2), 117–134. https://doi.org/10.1130/b25549.1

Hansen, L. N., & Warren, J. M. (2015). Quantifying the effect of pyroxene on deformation of peridotite in a natural shear zone. *Journal of Geophysical Research: Solid Earth*, *120*(4), 2717–2738. https://doi.org/10.1002/2014jb011584

Hansen, L. N., Zimmerman, M. E., & Kohlstedt, D. L. (2011). Grain boundary sliding in San Carlos olivine: Flow law parameters and crystallographic-preferred orientation. *Journal of Geophysical Research: Solid Earth*, *116*(B8), B08201. https://doi.org/10.1029/2011jb008220

Hidas, K., Garrido, C. J., Booth-Rea, G., Marchesi, C., Bodinier, J.-L., Dautria, J.-M., et al. (2019). Lithosphere tearing along STEP faults and synkinematic formation of lherzolite and wehrlite in the shallow subcontinental mantle. *Solid Earth Discussions*, 1-36. https://doi.org/10.5194/se-2019-32

Hielscher, R., & Schaeben, H. (2008). A novel pole figure inversion method: Specification of the MTEX algorithm. *Journal of Applied Crystallography*, *41*(6), 1024–1037. https://doi.org/10.1107/S0021889808030112

Holland, T., & Blundy, J. (1994). Non-ideal interactions in calcic amphiboles and their bearing on amphibole-plagioclase thermometry. *Contributions to Mineralogy and Petrology*, *116*(4), 433–447. https://doi.org/10.1007/bf00310910

Holland, T. J. B., & Powell, R. (2011). An improved and extended internally consistent thermodynamic dataset for phases of petrological interest, involving a new equation of state for solids. *Journal of Metamorphic Geology*, *29*(3), 333–383. https://doi.org/10.1111/j.1525-1314.2010.00923.x

Ildefonse, B., Lardeaux, J. M., & Caron, J. M. (1990). The behavior of shape preferred orientations in metamorphic rocks—Amphiboles and jadeites from the Monte Mucrone area (Sesia-Lanzo zone, Italian Western Alps). *Journal of Structural Geology*, *12*(8), 1005–1011. https://doi.org/10.1016/0191-8141(90)90096-H

Isacks, B., Oliver, J., & Sykes, L. R. (1968). Seismology and the new global tectonics. *Journal of Geophysical Research*, *73*(18), 5855–5899. https://doi.org/10.1029/JB073i018p05855

Jamtveit, B., Austrheim, H., & Malthe-Sørenssen, A. (2000). Accelerated hydration of the Earth's deep crust induced by stress perturbations. *Nature*, *408*(6808), 75–78. https://doi.org/10.1038/35040537

Jamtveit, B., Austrheim, H., & Putnis, A. (2016). Disequilibrium metamorphism of stressed lithosphere. *Earth-Science Reviews*, *154*, 1–13. https://doi.org/10.1016/j.earscirev.2015.12.002

Jamtveit, B., Ben-Zion, Y., Renard, F., & Austrheim, H. (2018). Earthquake-induced transformation of the lower crust. *Nature*, *556*(7702), 487–491. https://doi.org/10.1038/s41586-018-0045-y

Jamtveit, B., Petley-Ragan, A., Incel, S., Dunkel, K. G., Aupart, C., Austrheim, H., et al. (2019). The effects of earthquakes and fluids on the metamorphism of the lower continental crust. *Journal of Geophysical Research: Solid Earth*, *124*(8), 7725–7755. https://doi.org/10.1029/2018jb016461

Ji, S., Saruwatari, K., Mainprice, D., Wirth, R., Xu, Z., & Xia, B. (2003). Microstructures, petrofabrics and seismic properties of ultra high-pressure eclogites from Sulu region, China: Implications for rheology of subducted continental crust and origin of mantle reflections. *Tectonophysics*, *370*(1–4), 49–76.

Ji, S., Shao, T., Michibayashi, K., Long, C., Wang, Q., Kondo, Y., et al. (2013). A new calibration of seismic velocities, anisotropy, fabrics, and elastic moduli of amphibole-rich rocks. *Journal of Geophysical Research: Solid Earth*, *118*(9), 4699–4728. https://doi.org/10.1002/jgrb.50352

John, T., Medvedev, S., Rupke, L. H., Andersen, T. B., Podladchikov, Y. Y., & Austrheim, H. (2009). Generation of intermediate-depth earthquakes by self-localizing thermal runaway. *Nature Geoscience*, *2*(2), 137–140.

John, T., & Schenk, V. (2003). Partial eclogitisation of gabbroic rocks in a late Precambrian subduction zone (Zambia): Prograde metamorphism triggered by fluid infiltration. *Contributions to Mineralogy and Petrology*, *146*(2), 174–191.

Jung, H. (2017). Crystal preferred orientations of olivine, orthopyroxene, serpentine, chlorite, and amphibole, and implications for seismic anisotropy in subduction zones: A review. *Geosciences Journal*, *21*(6), 985–1011. https://doi.org/10.1007/s12303-017-0045-1

Jung, H., Green, H. W., & Dobrzhinetskaya, L. F. (2004). Intermediate-depth earthquake faulting by dehydration embrittlement with negative volume change. *Nature*, *428*(6982), 545–549. https://doi.org/10.1038/nature02412

Kaneko, Y., Maruyama, S., Terabayashi, M., Yamamoto, H., Ishikawa, M., Anma, R., et al. (2000). Geology of the Kokchetav UHP-HP metamorphic belt, Northern Kazakhstan. *Island Arc*, *9*(3), 264–283. https://doi.org/10.1046/j.1440-1738.2000.00278.x

Karato, S.-i. (2008). *Deforamtion of Earth materials—An introduction to the rheology of solid Earth*. New York, United States of America: Cambridge University Press.

Katayama, I., Nakashima, S., & Yurimoto, H. (2006). Water content in natural eclogite and implication for water transport into the deep upper mantle. *Lithos*, *86*(3–4), 245–259.

Keller, L. M., Götze, L. C., Rybacki, E., Dresen, G., & Abart, R. (2010). Enhancement of solid-state reaction rates by non-hydrostatic stress effects on polycrystalline diffusion kinetics. *American Mineralogist*, *95*(10), 1399–1407. https://doi.org/10.2138/am.2010.3372

Keppler, R. (2018). Crystallographic preferred orientations in eclogites—A review. *Journal of Structural Geology*, *115*, 284–296. https://doi.org/10.1016/j.jsg.2018.04.003

Keppler, R., Behrmann, J. H., & Stipp, M. (2017). Textures of eclogites and blueschists from Syros island, Greece: Inferences for elastic anisotropy of subducted oceanic crust. *Journal of Geophysical Research: Solid Earth*, *122*(7), 5306–5324. https://doi.org/10.1002/2017JB014181

Keppler, R., Stipp, M., Behrmann, J. H., Ullemeyer, K., & Heidelbach, F. (2016). Deformation inside a paleosubduction channel—Insights from microstructures and crystallographic preferred orientations of eclogites and metasediments from the Tauern Window, Austria. *Journal of Structural Geology*, *82*, 60–79. https://doi.org/10.1016/j.jsg.2015.11.006

Keppler, R., Ullemeyer, K., Behrmann, J. H., Stipp, M., Kurzawski, R. M., & Lokajíček, T. (2015), Crystallographic preferred orientations of exhumed subduction channel rocks from the Eclogite Zone of the Tauern Window (Eastern Alps, Austria), and implications on rock elastic anisotropies at great depths, *Tectonophysics*, *647-648*(0), 89–104, https://doi.org/10.1016/j.tecto.2015.02.011.

Kitamura, K. (2006). Constraint of lattice-preferred orientation (LPO) on Vp anisotropy of amphibole-rich rocks. *Geophysical Journal International*, *165*(3), 1058–1065. https://doi.org/10.1111/j.1365-246X.2006.02961.x

Kohlstedt, D. L., Evans, B., & Mackwell, S. J. (1995). Strength of the lithosphere: Constraints imposed by laboratory experiments. *Journal of Geophysical Research: Solid Earth*, *100*(B9), 17,587–17,602. https://doi.org/10.1029/95jb01460

Krogh, T. E., Kamo, S. L., Robinson, P., Terry, M. P., & Kwok, K. (2011). U–Pb zircon geochronology of eclogites from the Scandian Orogen, northern Western Gneiss Region, Norway: 14–20 million years between eclogite crystallization and return to amphibolite-facies conditions. *Canadian Journal of Earth Sciences*, *48*(2), 441–472. https://doi.org/10.1139/E10-076

Kurz, W., Jansen, E., Hundenborn, R., Pleuger, J., Schafer, W., & Unzog, W. (2004). Microstructures and crystallographic preferred orientations of omphacite in Alpine eclogites: Implications for the exhumation of (ultra-) high-pressure units. *Journal of Geodynamics*, *37*(1), 1–55. https://doi.org/10.1016/j.jog.2003.10.001

Kylander-Clark, A. R. C., Hacker, B. R., Johnson, C. M., Beard, B. L., Mahlen, N. J., & Lapen, T. J. (2007). Coupled Lu–Hf and Sm–Nd geochronology constrains prograde and exhumation histories of high- and ultrahigh-pressure eclogites from western Norway. *Chemical Geology*, *242*(1–2), 137–154. https://doi.org/10.1016/j.chemgeo.2007.03.006

Langdon, T. (2006). Grain boundary sliding revisited: Developments in sliding over four decades. *Journal of Materials Science*, *41*(3), 597–609. https://doi.org/10.1007/s10853-006-6476-0

Laurent, V., Jolivet, L., Roche, V., Augier, R., Scaillet, S., & Cardello, G. L. (2016). Strain localization in a fossilized subduction channel: Insights from the Cycladic Blueschist Unit (Syros, Greece). *Tectonophysics*, *672*, 150–169. https://doi.org/10.1016/j.tecto.2016.01.036

Linckens, J. (2010), Microfabric evolution and strain localization in the naturally deformed mantle rocks, 160 pp, University of Bern.

Linckens, J., Bruijn, R. H. C., & Skemer, P. (2014), Dynamic recrystallization and phase mixing in experimentally deformed peridotite, *Earth and Planetary Science Letters*, *388*(0), 134–142, doi:https://doi.org/10.1016/j.epsl.2013.11.037.

Linckens, J., Herwegh, M., & Müntener, O. (2015), Small quantity but large effect—How minor phases control strain localization in upper mantle shear zones, *Tectonophysics*, *643*(0), 26–43, doi:https://doi.org/10.1016/j.tecto.2014.12.008.

Linckens, J., Herwegh, M., Muntener, O., & Mercolli, I. (2011). Evolution of a polymineralic mantle shear zone and the role of second phases in the localization of deformation. *Journal of Geophysical Research: Solid Earth*, *116*(B6), B06210. https://doi.org/10.1029/2010jb008119

Liou, J. G., Zhang, R. Y., & Jahn, B.-M. (2000). Petrological and geochemical characteristics of ultrahigh-pressure metamorphic rocks from the Dabie-Sulu terrane, east-central China. *International Geology Review*, *42*(4), 328–352. https://doi.org/10.1080/00206810009465086

Luisier, C., Baumgartner, L., Schmalholz, S. M., Siron, G., & Vennemann, T. (2019). Metamorphic pressure variation in a coherent Alpine nappe challenges lithostatic pressure paradigm. *Nature Communications*, *10*(1), 4734. https://doi.org/10.1038/s41467-019-12727-z

Lund, M. G., & Austrheim, H. (2003). High-pressure metamorphism and deep-crustal seismicity: Evidence from contemporaneous formation of pseudotachylytes and eclogite facies coronas. *Tectonophysics*, *372*(1–2), 59–83. https://doi.org/10.1016/S0040-1951(03)00232-4

MacGregor, I. D., & Manton, W. I. (1986). Roberts victor eclogites: Ancient oceanic crust. *Journal of Geophysical Research: Solid Earth*, *91*(B14), 14,063–14,079. https://doi.org/10.1029/JB091iB14p14063

Mainprice, D., Bascou, J., Cordier, P., & Tommasi, A. (2004), Crystal preferred orientations of garnet: comparison between numerical simulations and electron back-scattered diffraction (EBSD) measurements in naturally deformed eclogites, in *Journal of Structural Geology*, *26*(11) edited, pp. 2089–2102.

Mancktelow, N. S. (2008). Tectonic pressure: Theoretical concepts and modelled examples. *Lithos*, *103*(1–2), 149–177. https://doi.org/10.1016/j.lithos.2007.09.013

Mansard, N., Stünitz, H., Raimbourg, H., & Précigout, J. (2020). The role of deformation-reaction interactions to localize strain in poly-mineralic rocks: Insights from experimentally deformed plagioclase-pyroxene assemblages. *Journal of Structural Geology*, *134*, 104,008. https://doi.org/10.1016/j.jsg.2020.104008

Maruyama, G., & Hiraga, T. (2017a). Grain- to multiple-grain-scale deformation processes during diffusion creep of forsterite + diopside aggregate: 1. *Direct observations, Journal of Geophysical Research: Solid Earth*, *122*(8), 5890–5915. https://doi.org/10.1002/2017jb014254

Maruyama, G., & Hiraga, T. (2017b). Grain- to multiple-grain-scale deformation processes during diffusion creep of forsterite + diopside aggregate: 2. Grain boundary sliding-induced grain rotation and its role in crystallographic preferred orientation in rocks. *Journal of Geophysical Research: Solid Earth*, *122*(8), 5916–5934. https://doi.org/10.1002/2017jb014255

Masuda, T., Michibayashi, K., & Ohta, H. (1995). Shape preferred orientation of rigid particles in a viscous matrix—Reevaluation to determine kinematic parameters of ductile deformation. *Journal of Structural Geology*, *17*(1), 115–129. https://doi.org/10.1016/0191-8141(94)E0026-U

Miyazaki, T., Sueyoshi, K., & Hiraga, T. (2013). Olivine crystals align during diffusion creep of Earth's upper mantle. *Nature*, *502*(7471), 321−+. https://doi.org/10.1038/Nature12570

Molina, J. F., Moreno, J. A., Castro, A., Rodriguez, C., & Fershtater, G. B. (2015). Calcic amphibole thermobarometry in metamorphic and igneous rocks: New calibrations based on plagioclase/amphibole Al-Si partitioning and amphibole/liquid mg partitioning. *Lithos*, *232*, 286–305. https://doi.org/10.1016/j.lithos.2015.06.027

Mørk, M. B. E. (1985). A gabbro to eclogite transition on Flemsøy, Sunnmøre, western Norway. *Chemical Geology*, *50*(1–3), 283–310. https://doi.org/10.1016/0009-2541(85)90125-1

Mørk, M. B. E. (1986). Coronite and eclogite formation in olivine gabbro (Western Norway). *Reaction paths and garnet zoning Mineralogical Magazine*, *50*, 417–426. https://doi.org/10.1180/minmag.1986.050.357.0

Mørk, M. B. E., & Mearns, E. W. (1986). Sm-Nd isotopic systematics of a gabbro-eclogite transition. *Lithos*, *19*(3–4), 255–267. https://doi.org/10.1016/0024-4937(86)90026-5

Neufeld, K., Ring, U., Heidelbach, F., Dietrich, S., & Neuser, R. D. (2008). Omphacite textures in eclogites of the Tauern Window: Implications for the exhumation of the Eclogite Zone, Eastern Alps. *Journal of Structural Geology*, *30*(8), 976–992. https://doi.org/10.1016/j.jsg.2008.03.010

Newman, J., Lamb, W. M., Drury, M. R., & Vissers, R. L. M. (1999). Deformation processes in a peridotite shear zone: Reaction-softening by an H_2O-deficient, continuous net transfer reaction. *Tectonophysics*, *303*(1–4), 193–222. https://doi.org/10.1016/s0040-1951(98)00259-5

Oleskevich, D. A., Hyndman, R. D., & Wang, K. (1999). The updip and downdip limits to great subduction earthquakes: Thermal and structural models of Cascadia, south Alaska, SW Japan, and Chile. *Journal of Geophysical Research: Solid Earth*, *104*(B7), 14,965–14,991. https://doi.org/10.1029/1999JB900060

Palin, R. M., Reuber, G. S., White, R. W., Kaus, B. J. P., & Weller, O. M. (2017). Subduction metamorphism in the Himalayan ultrahigh-pressure Tso Morari massif: An integrated geodynamic and petrological modelling approach. *Earth and Planetary Science Letters*, *467*, 108–119. https://doi.org/10.1016/j.epsl.2017.03.029

Park, M., & Jung, H. (2019). Relationships between eclogite-facies mineral assemblages, deformation microstructures, and seismic properties in the Yuka terrane, North Qaidam ultrahigh-pressure metamorphic belt, NW China. *Journal of Geophysical Research: Solid Earth*, *124*(12), 13,168–13,191. https://doi.org/10.1029/2019jb018198

Passchier, C. W. (1987). Stable positions of rigid objects in non-coaxial flow—A study in vorticity analysis. *Journal of Structural Geology*, *9*(5–6), 679–690. https://doi.org/10.1016/0191-8141(87)90152-0

Passchier, C. W., & Trouw, R. A. J. (2005). *Microtectonics* (2nd ed.). New York: Springer.

Peacock, S. M. (1993). The importance of blueschist → eclogite dehydration reactions in subducting oceanic crust. *Geological Society of America Bulletin*, *105*(5), 684–694. https://doi.org/10.1130/0016-7606(1993)105<0684:tiobed>2.3.co;2

Petley-Ragan, A., Ben-Zion, Y., Austrheim, H., Ildefonse, B., Renard, F., & Jamtveit, B. (2019). Dynamic earthquake rupture in the lower crust. *Science Advances*, *5*(7), eaaw0913. https://doi.org/10.1126/sciadv.aaw0913

Petley-Ragan, A., Dunkel, K. G., Austrheim, H., Ildefonse, B., & Jamtveit, B. (2018). Microstructural records of earthquakes in the lower crust and associated fluid-driven metamorphism in plagioclase-rich granulites. *Journal of Geophysical Research: Solid Earth*, *123*(5), 3729–3746. https://doi.org/10.1029/2017jb015348

Pleuger, J., & Podladchikov, Y. Y. (2014). A purely structural restoration of the NFP20-East cross section and potential tectonic overpressure in the Adula nappe (central Alps). *Tectonics*, *33*(5), 656–685. https://doi.org/10.1002/2013TC003409

Précigout, J., & Hirth, G. (2014). B-type olivine fabric induced by grain boundary sliding. *Earth and Planetary Science Letters*, *395*, 231–240. https://doi.org/10.1016/j.epsl.2014.03.052

Precigout, J., Prigent, C., Palasse, L., & Pochon, A. (2017). Water pumping in mantle shear zones. *Nature Communications*, *8*(1), 1–10. https://doi.org/10.1038/ncomms15736

Prigent, C., Guillot, S., Agard, P., & Ildefonse, B. (2018). Fluid-assisted deformation and strain localization in the cooling mantle wedge of a young subduction zone (Semail ophiolite). *Journal of Geophysical Research: Solid Earth*, *123*(9), 7529–7549. https://doi.org/10.1029/2018jb015492

Putnis, A., Jamtveit, B., & Austrheim, H. (2017). Metamorphic processes and seismicity: The Bergen Arcs as a natural laboratory. *Journal of Petrology*, *58*(10), 1871–1898. https://doi.org/10.1093/petrology/egx076

Renedo, R. N., Nachlas, W. O., Whitney, D. L., Teyssier, C., Piazolo, S., Gordon, S. M., & Fossen, H. (2015). Fabric development during exhumation from ultrahigh-pressure in an eclogite-bearing shear zone, Western Gneiss Region, Norway. *Journal of Structural Geology*, *71*, 58–70. https://doi.org/10.1016/j.jsg.2014.09.012

Reuber, G., Kaus, B. J. P., Schmalholz, S. M., & White, R. W. (2016). Nonlithostatic pressure during subduction and collision and the formation of (ultra)high-pressure rocks. *Geology*, *44*(5), 343–346. https://doi.org/10.1130/g37595.1

Richter, B., Stünitz, H., & Heilbronner, R. (2016). Stresses and pressures at the quartz-to-coesite phase transformation in shear deformation experiments. *Journal of Geophysical Research: Solid Earth*, *121*(11), 8015–8033. https://doi.org/10.1002/2016jb013084

Root, D. B., Hacker, B. R., Mattinson, J. M., & Wooden, J. L. (2004). Zircon geochronology and ca. 400 Ma exhumation of Norwegian ultrahigh-pressure rocks: An ion microprobe and chemical abrasion study. *Earth and Planetary Science Letters*, *228*(3–4), 325–341. https://doi.org/10.1016/j.epsl.2004.10.019

Schmalholz, S. M., & Podladchikov, Y. (2014). Metamorphism under stress: The problem of relating minerals to depth. *Geology*, *42*(8), 733–734. https://doi.org/10.1130/focus0822014.1

Schulmann, K., Konopasek, J., Janousek, V., Lexa, O., Lardeaux, J. M., Edel, J. B., et al. (2009). An Andean type Palaeozoic convergence in the Bohemian Massif. *Comptes Rendus Geoscience*, *341*(2–3), 266–286. https://doi.org/10.1016/j.crte.2008.12.006

Sheng, Y. M., Xia, Q. K., Dallai, L., Yang, X. Z., & Hao, Y. T. (2007). H_2O contents and D/H ratios of nominally anhydrous minerals from ultrahigh-pressure eclogites of the Dabie orogen, eastern China. *Geochimica et Cosmochimica Acta*, *71*(8), 2079–2103. https://doi.org/10.1016/j.gca.2007.01.018

Skemer, P., Katayama, B., Jiang, Z. T., & Karato, S. (2005). The misorientation index: Development of a new method for calculating the strength of lattice-preferred orientation. *Tectonophysics*, *411*(1–4), 157–167. https://doi.org/10.1016/j.tecto.2005.08.023

Soldner, J., Oliot, E., Schulmann, K., Štípská, P., Kusbach, V., & Anczkiewicz, R. (2017). Metamorphic *P–T–t–d* evolution of (U)HP metabasites from the South Tianshan accretionary complex (NW China)—Implications for rock deformation during exhumation in a subduction channel. *Gondwana Research*, *47*, 161–187. https://doi.org/10.1016/j.gr.2016.07.007

Song, S. G., Zhang, L. F., Niu, Y. L., Wei, C. J., Liou, J. G., & Shu, G. M. (2007). Eclogite and carpholite-bearing metasedimentary rocks in the North Qilian suture zone, NW China: Implications for early palaeozoic cold oceanic subduction and water transport into mantle. *Journal of Metamorphic Geology*, *25*(5), 547–563. https://doi.org/10.1111/j.1525-1314.2007.00713.x

Spandler, C., Hermann, J., Faure, K., Mavrogenes, J. A., & Arculus, R. J. (2008). The importance of talc and chlorite "hybrid" rocks for volatile recycling through subduction zones; evidence from the high-pressure subduction mélange of New Caledonia. *Contributions to Mineralogy and Petrology*, *155*(2), 181–198. https://doi.org/10.1007/s00410-007-0236-2

Sundberg, M., & Cooper, R. F. (2008). Crystallographic preferred orientation produced by diffusional creep of harzburgite: Effects of chemical interactions among phases during plastic flow. *Journal of Geophysical Research: Solid Earth*, *113*, 1–16. https://doi.org/10.1029/2008jb005618

Tasaka, M., & Hiraga, T. (2013). Influence of mineral fraction on the rheological properties of forsterite + enstatite during grain-size-sensitive creep: 1. Grain size and grain growth laws. *Journal of Geophysical Research: Solid Earth*, *118*(8), 3970–3990. https://doi.org/10.1002/jgrb.50285

Tasaka, M., Hiraga, T., & Michibayashi, K. (2014). Influence of mineral fraction on the rheological properties of forsterite + enstatite during grain size sensitive creep: 3. Application of grain growth and flow laws on peridotite ultramylonite. *Journal of Geophysical Research: Solid Earth*, *119*(2), 840–857. https://doi.org/10.1002/2013jb010619

Tatham, D. J., Lloyd, G. E., Butler, R. W. H., & Casey, M. (2008). Amphibole and lower crustal seismic properties. *Earth and Planetary Science Letters*, *267*(1–2), 118–128. https://doi.org/10.1016/j.epsl.2007.11.042

Terry, M. P., & Heidelbach, F. (2006). Deformation-enhanced metamorphic reactions and the rheology of high-pressure shear zones, Western Gneiss Region, Norway. *Journal of Metamorphic Geology*, *24*(1), 3–18. https://doi.org/10.1111/j.1525-1314.2005.00618.x

Terry, M. P., & Robinson, P. (2003). Evolution of amphibolite-facies structural features and boundary conditions for deformation during exhumation of high- and ultrahigh-pressure rocks, Nordøyane, Western Gneiss Region, Norway. *Tectonics*, *22*(4), 1–23. https://doi.org/10.1029/2001TC001349

Terry, M. P., & Robinson, P. (2004). Geometry of eclogite-facies structural features: Implications for production and exhumation of ultrahigh-pressure and high-pressure rocks, Western Gneiss Region, Norway. *Tectonics*, *23*(2), 1–23. https://doi.org/10.1029/2002TC001401

Terry, M. P., Robinson, P., & Ravna, E. J. K. (2000). Kyanite eclogite thermobarometry and evidence for thrusting of UHP over HP metamorphic rocks, Nordøyane, Western Gneiss Region, Norway. *American Mineralogist*, *85*(11–12), 1637–1650. https://doi.org/10.2138/am-2000-11-1207

Thompson, A. B., Rubie, D. C., & Bayly, M. B. (1985). Metamorphic reactions: Kinetics, textures, and deformation. In *Advances in physical geochemistry, v. 4, Edited* (291 pp.). New York: Springer-Verlag.

Tichelaar, B. W., & Ruff, L. J. (1993). Depth of seismic coupling along subduction zones. *Journal of Geophysical Research: Solid Earth*, *98*(B2), 2017–2037. https://doi.org/10.1029/92JB02045

Tucker, R. D., Robinson, P., Solli, A., Gee, D. G., Thorsnes, T., Krogh, T. E., et al. (2004). Thrusting and extension in the Scandian Hinterland, Norway: New U-Pb ages and tectonostratigraphic evidence. *American Journal of Science*, *304*(6), 477–532. https://doi.org/10.2475/ajs.304.6.477

Van der Wal, D., Chopra, P., Drury, M., & Gerald, J. F. (1993). Relationships between dynamically recrystallized grain size and deformation conditions in experimentally deformed olivine rocks. *Geophysical Research Letters*, *20*(14), 1479–1482. https://doi.org/10.1029/93GL01382

van Roermund, H. L. M., & Drury, M. R. (1998). Ultra-high pressure (*P* > 6 GPa) garnet peridotites in Western Norway: Exhumation of mantle rocks from >185 km depth. *Terra Nova*, *10*(6), 295–301. https://doi.org/10.1046/j.1365-3121.1998.00213.x

Viete, D. R., Hacker, B. R., Allen, M. B., Seward, G. G. E., Tobin, M. J., Kelley, C. S., et al. (2018). Metamorphic records of multiple seismic cycles during subduction. *Science Advances*, *4*(3), eaaq0234. https://doi.org/10.1126/sciadv.aaq0234

Vrijmoed, J. C., & Podladchikov, Y. Y. (2015). Thermodynamic equilibrium at heterogeneous pressure. *Contributions to Mineralogy and Petrology*, *170*(1), 1–27. https://doi.org/10.1007/s00410-015-1156-1

Vrijmoed, J. C., Smith, D. C., & Van Roermund, H. L. M. (2008). Raman confirmation of microdiamond in the Svartberget Fe-Ti type garnet peridotite, Western Gneiss Region, Western Norway. *Terra Nova*, *20*(4), 295–301. https://doi.org/10.1111/j.1365-3121.2008.00820.x

Wain, A., Waters, D., Jephcoat, A., & Olijynk, H. (2000). The high-pressure to ultrahigh-pressure eclogite transition in the Western Gneiss Region, Norway. *European Journal of Mineralogy*, *12*(3), 667–687. https://doi.org/10.1127/0935-1221/2000/0012-0667

Walsh, E. O., Hacker, B. R., Gans, P. B., Grove, M., & Gehrels, G. (2007). Protolith ages and exhumation histories of (ultra)high-pressure rocks across the Western Gneiss Region, Norway. *Geological Society of America Bulletin*, *119*(3–4), 289–301. https://doi.org/10.1130/b25817.1

Wang, Y. F., Zhang, J. F., & Shi, F. (2013), The origin and geophysical implications of a weak C-type olivine fabric in the Xugou ultrahigh pressure garnet peridotite, *Earth and Planetary Science Letters*, *376*(0), 63–73, https://doi.org/10.1016/j.epsl.2013.06.017.

Wark, D. A., & Watson, E. B. (2000). Effect of grain size on the distribution and transport of deep-seated fluids and melts. *Geophysical Research Letters*, *27*(14), 2029–2032. https://doi.org/10.1029/2000GL011503

Warren, J. M., & Hirth, G. (2006). Grain size sensitive deformation mechanisms in naturally deformed peridotites. *Earth and Planetary Science Letters*, *248*(1–2), 438–450. https://doi.org/10.1016/j.epsl.2006.06.006

Wassmann, S., & Stockhert, B. (2013), Rheology of the plate interface—Dissolution precipitation creep in high pressure metamorphic rocks, *Tectonophysics*, *608*(0), 1–29, https://doi.org/10.1016/j.tecto.2013.09.030.

Wheeler, J. (2014). Dramatic effects of stress on metamorphic reactions. *Geology*, *42*(8), 647–650. https://doi.org/10.1130/g35718.1

White, R. W., Powell, R., Holland, T. J. B., Johnson, T. E., & Green, E. C. R. (2014). New mineral activity–composition relations for thermodynamic calculations in metapelitic systems. *Journal of Metamorphic Geology*, *32*(3), 261–286. https://doi.org/10.1111/jmg.12071

White, R. W., Powell, R., & Johnson, T. E. (2014). The effect of Mn on mineral stability in metapelites revisited: New a–x relations for manganese-bearing minerals. *Journal of Metamorphic Geology*, *32*(8), 809–828. https://doi.org/10.1111/jmg.12095

Wu, X., Meng, D., Fan, X., Meng, X., Zheng, J., & Mason, R. (2008), Defect microstructures in garnet, omphacite and symplectite from UHP eclogites, eastern Dabieshan, China: A TEM and FTIR study, in *Mineralogical Magazine*, edited, p. 1057, https://doi.org/10.1180/minmag.2008.072.5.1057.

Yamato, P., & Brun, J. P. (2017). Metamorphic record of catastrophic pressure drops in subduction zones. *Nature Geoscience*, *10*(1), 46–50. https://doi.org/10.1038/Ngeo2852

Yang, J., Xu, Z., Zhang, J., Song, S., Wu, C., Shi, R., et al. (2002). Early Palaeozoic North Qaidam UHP metamorphic belt on the north-eastern Tibetan plateau and a paired subduction model. *Terra Nova*, *14*(5), 397–404. https://doi.org/10.1046/j.1365-3121.2002.00438.x

Yao, Z., Qin, K., Wang, Q., & Xue, S. (2019). Weak B-type olivine fabric induced by fast compaction of crystal mush in a crustal magma reservoir. *Journal of Geophysical Research: Solid Earth*, *124*(4), 3530–3556. https://doi.org/10.1029/2018jb016728

Zhao, N., Hirth, G., Cooper, R. F., Kruckenberg, S. C., & Cukjati, J. (2019). Low viscosity of mantle rocks linked to phase boundary sliding. *Earth and Planetary Science Letters*, *517*, 83–94. https://doi.org/10.1016/j.epsl.2019.04.019